TECHNISCHE UNIVERSITÄT WIEN

Stochastic Snap-Through Dynamics of Bistable MEMS

DIPLOMA THESIS

submitted in partial fulfillment of the requirements for the degree of

Diplom-Ingenieur

in

Embedded Systems

by

Maximilian Franz Kern, BSc
Registration Number 11731658

to the Faculty of Electrical Engineering and Information Technology

at the TU Wien

Advisor: Univ.Prof. Dipl.-Phys. Dr.rer.nat. Ulrich Schmid
Co-Advisor: Univ.Ass. Daniel Platz, MSc PhD

Vienna, 22nd November, 2023

Maximilian Franz Kern | Ulrich Schmid

Technische Universität Wien
A-1040 Wien ▪ Karlsplatz 13 ▪ Tel. +43-1-58801-0 ▪ www.tuwien.at

Declaration of Authorship

Maximilian Franz Kern, BSc

I hereby declare that I have written this Diploma Thesis independently, that I have completely specified the utilized sources and resources and that I have definitely marked all parts of the work - including tables, maps and figures - which belong to other works or to the internet, literally or extracted, by referencing the source as borrowed.

Vienna, 22nd November, 2023

Maximilian Franz Kern

Kurzfassung

Mikroelektromechanische Systeme (MEMS) sind weit verbreitet in unserem Alltag, von Sensoren in Smartphones bis hin zu Anwendungen in der Industrie. Bistabile MEMS, eine Untergruppe von MEMS, können durch externe Anregung von einem stabilen Zustand in einen anderen umgeschaltet werden. Mit zunehmend kleineren Geometrien steigt der Einfluss von Rauschen. Experimente mit bistabilen MEMS-Platten haben stochastisches Verhalten in Bezug auf ihre endgültige Ablenkung nach einer definierten Anzahl von Anregungsimpulsen gezeigt. In dieser Arbeit erweitern wir ein bestehendes von-Karman-Plattenmodell um Rauschterme, um die Auswirkungen von Temperatur und durch eine Piezoschicht verursachtem Rauschen zu berücksichtigen, die als Aktuator dient. Wir präsentieren die Theorie der stochastischen Differentialgleichungen sowie Methoden zu ihrer numerischen Lösung. Außerdem untersuchen wir die Eigenschaften solcher bistabilen Systeme. Unsere Untersuchungen zeigen, dass bei Platten in der Größe der derzeit in Experimenten untersuchten der Einfluss von temperaturbedingtem Rauschen nicht signifikant ist. Durch Modellierung des Rauschens in der Piezolage zeigt unser Modell eine höhere Robustheit gegenüber Rauschen bei höheren mechanischen Vorspannungen. Die endgültige Ablenkung der Platte, die durch eine endliche Anzahl von Impulsen angeregt wird, hängt nicht nur deterministisch von der Anregungsfrequenz und -amplitude ab, sondern ist auch ein stochastischer Prozess. Die Ergebnisse zeigen, dass der Einfluss von Rauschen in einem bestimmten Bereich von Parametern höher ist und gleichzeitig Bereiche bietet, die robuster gegenüber Rauschen sind als andere. Wir untersuchen auch die stochastische Resonanz der Platte und bestimmen die mittlere Fluchtrate. Bei der Untersuchung, ob sich der Zustand der Platte nach einer Anregung für verschiedene Amplituden und Frequenzen geändert hat, zeigt sich, dass Rauschen hauptsächlich entlang der Grenze zwischen den Bereichen sichtbar ist, in denen ein Zustandswechsel stattfindet oder nicht. Diese Grenzfläche dehnt sich bei höheren Rauschintensitäten aus. Wir zeigen auch, wie die klar definierten Bereiche bei zunehmender Anzahl von Impulsen kleiner werden, was einen gewünschten, rauschrobusten Betrieb deutlich erschwert.

Abstract

Micro-Electro-Mechanical Systems (MEMS) are widely spread in our lives, ranging from sensor appliances in smartphones to appliances in industry. Bistable MEMS, a subset of MEMS, can be switched from one stable state to another by external excitation. As geometries become smaller and smaller, the influence of noise rises. Experiments on bistable MEMS plates have shown stochastic behaviour concerning their final deflection after a defined amount of excitation pulses. Here, we expand a existing von Karman plate model with noise terms to account for the effects of temperature and noise induced by a piezo layer, which acts as an actuator. We present the theory of stochastic differential equations, including methods to numerically solve them. We also look into the properties of such bistable systems. This work finds for plates as large as those currently investigated in experiments that the impact of temperature induced noise is not significant. Modelling noise in the piezo layer, our model shows higher robustness against noise for higher pre-stresses. The final deflection of the plate, excited by a finite number of pulses, depends not only deterministically on the excitation frequency and amplitude but is also a stochastic process. The results show that the influence of noise is higher for a specific range of parameters, in the contrary offering areas which are more noise robust than others. We also investigate stochastic resonance of the plate and determined the mean escape rate. When exploring whether the state of the plate changed after an excitation for various amplitudes and frequencies, results show that noise is primarily visible along the boarder between the areas of a state change happening or not, with the boarder area expanding for higher noise intensities. We also demonstrate how the clearly defined areas get smaller for an increasing number of pulses, making a wanted noise robust operation much more challenging.

Contents

Chapter 1

Introduction

MEMS (Micro-Electro-Mechanical Systems) are widely spread in our lives, ranging from sensor appliances in smartphones to appliances in industrial sectors. Bistable MEMS, a subset of MEMS, have two stable static deflection states at the same time. An example for these types of MEMS are buckled clamped plates. During fabrication processes, permanent static compressive stress is induced, resulting in the plate having at least two stable buckling states - either buckling up or down. A key objective in bistable MEMS is the efficient initiation of snap-throughs, switching the plate from one stable state to another. The mechanical deflection up to tens of micrometers during this snap-through process greatly exceeds typical oscillation amplitudes below one micrometer of conventional resonant MEMS. What is more, snap-through can be achieved by integrating a piezoelectric thin film, enabling to induce stress into the structure which initiates a snap-through.

Recently, noise has gained attention in studies of bistable MEMS, particularly the case in the field of energy harvesters [4, 20]. Additionally, numerical methods have been further developed, opening the use of stochastic methods for applied sciences [18].

Concerning bistable MEMS with two-dimensional plate geometries, experimental data of exciting plates via a piezo layer have been published [2]. A model based on the von Karman plate model has been presented to describe the static and dynamic behaviour of bistable MEMS [3].

Measurements have shown that plates exhibit a stochastic behaviour, which raises questions about the role of noise and its influence. Measurement results are shown in figure 1.1. The results show the number of observed snap-throughs in a series of ten measurements. In each of the measurements the plate was excited by the same finite voltage pulse train characterized by an excitation amplitude and frequency. Even though the starting position of the plates and the excitation signal is each

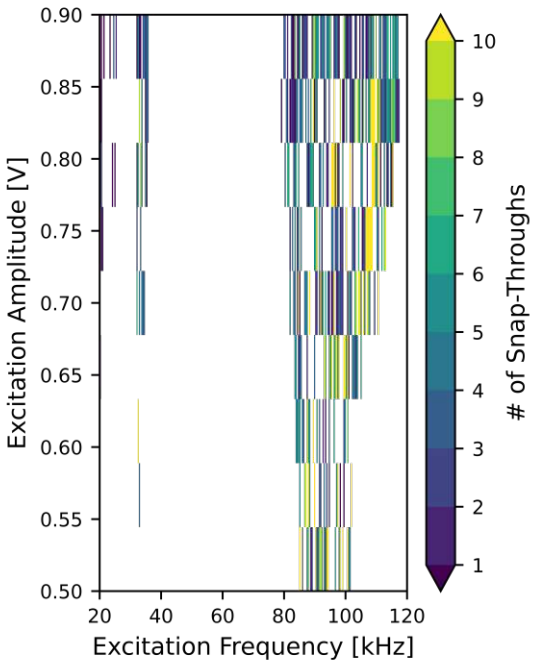

Figure 1.1: Measured number of state changes after an excitation out of ten runs as a function of the piezo-voltage amplitude and frequency. The number of excitation pulses is the same for each frequency. [13]

time the same, the final deflection, described as snap-through, varies [13]. In the paper, the term snap-through is used to describe a state change after an excitation, but in this work we will define it as every time the plate changes its deflection state. In these situations, noise can be especially important, as this state changes are highly nonlinear.

Regarding the influence of noise in geometrically small systems, a cantilever beam can serve as a motivational example. Considering a cantilever beam (figure 1.2) mounted at $x = 0$ with its width w much smaller than its length L, its spring constant k is calculated by

$$k = \frac{Ewt^3}{4L^3} \tag{1.1}$$

with Young's module E and its thickness t.

At finite temperatures the system is subject to thermal noise which is quantified by the equipartition theorem. May the deflection $w(x,t)$ be

$$w(x,t) = \sum_i x_i(t)\phi_i(x) \tag{1.2}$$

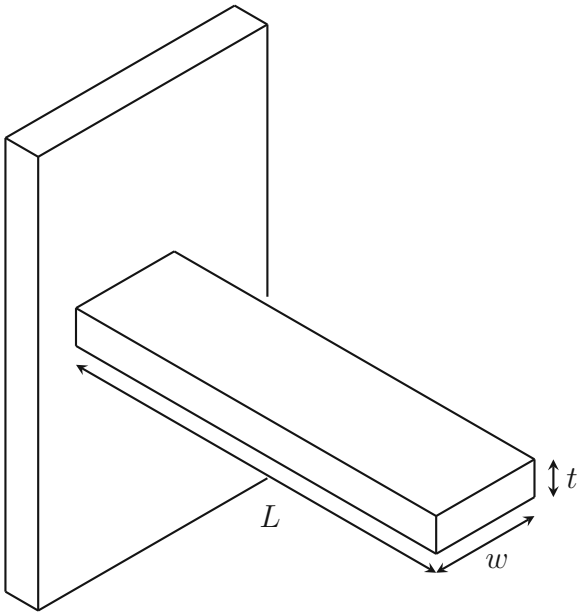

Figure 1.2: Cantilever beam

with the mode coefficients x_i and basis functions ϕ_i. Considering only the first mode and assuming its spring constant $k_1 = k$, the equipartition theorem relates the temperature T of the system to the average potential energy of the first mode

$$\frac{1}{2}k_1\langle x_1^2\rangle = \frac{k_B T}{2} \tag{1.3}$$

with the Boltzmann constant k_B. To understand the influence of thermal noise on the dynamics, we study how the relative magnitude of the thermal noise in the system changes as the system size is changed. Scaling the dimensions of the beam with the factor λ

$$L' = L/\lambda, \quad w' = w/\lambda, \quad t' = t/\lambda \tag{1.4}$$

results in the scaled spring constant of

$$k_1' = \frac{k_1}{\lambda}. \tag{1.5}$$

Inserting equation 1.5 in 1.3, for constant temperatures, the mean square displacement scales by

$$\langle x_1^2\rangle' = \lambda\langle x_1^2\rangle. \tag{1.6}$$

This means that for smaller geometries, the temperature induced movement grows accordingly. Used parameters and results are shown in tables 1.1 and 1.2. It is an example for why temperature induced noise is much more significant for MEMS and the reason for this thesis.

L[m]	t[m]	w[m]	E[GPa]	T[K]
1	0.01	0.1	169	293

Table 1.1: Used parameters to describe the cantilever beam.

λ	k_1	$\langle x_1^2 \rangle$
1	4225	9.57e-25
1×10^3	4.225	9.57e-22
1×10^6	4.225e-3	9.57e-19
1×10^9	4.225e-6	9.57e-16

Table 1.2: Average movement $\langle x_1^2 \rangle$ of cantilever beam using different scaling factors λ. Lower dimensions lead to lower stiffness k_1 and result therefore in higher average movement.

In order to ensure the desired behaviour of the MEMS plate, noise has to be taken into account.

The goal of this work is to investigate the effect of noise on the bistable MEMS plate. To achieve this, we introduce a framework to simulate the plate's behaviour under the influence of noise. The implemented model is based on a previously presented Galerkin approach that solves the von Karman plate model. In this thesis, the model is further developed by considering noise, including noise induced by temperature and noise in the piezo layer, which effectively changes the stress induced by an excitation. We discuss equations with additional terms describing noise, called stochastic differential equations. Different numerical methods to solve the resulting stochastic differential equations are presented and validated. Furthermore, the bistability of the plate is investigated and analysed by taking means of stochastic measures. Finally, we discuss the path moving forward concerning real-life experiments and proposing interesting new measurements, which include investigating whether the state of the plate changes after a low number of pulses and what impact noise has on this process.

Chapter 2

Theoretical Basics

2.1 Stochastic Differential Equations (SDEs)

In order to analyse the dynamic behaviour of bistable MEMS actuators under the influence of noise, we need certain tools to describe that influence. A well known tool is the Stochastic Differential Equation (SDE). A rather simple example of an SDE is the Langevin equation [5]

$$\frac{dx}{dt} = a(x,t) + b(x,t)\xi(t) \tag{2.1}$$

where x is the position variable. The function $a(x,t)$ represents a function dependent on x and t, as is function $b(x,t)$, but with the speciality of its multiplication with a time dependent noise term $\xi(t)$. The noise term are random fluctuations, resulting of incremental changes of a random variable. For $b(x,t) = 0$, the equation is purely deterministic and solutions are obtained by standard integration techniques. In contrast, with the whole equation in question, a way of integrating the stochastic term has to be defined. This leads to the stochastic integral, which will be investigated in 2.1.2. But first we will investigate the noise term $\xi(t)$.

2.1.1 Brownian Motion

Looking into the noise term, it is further described as a Wiener process with the following characteristics [7]: The standard Wiener process over the time interval $[0,T]$ is a random variable $W(t)$ that depends continuously on $t \in [0,T]$ and satisfies the following conditions

- $W_0 = W(0) = 0$

- The random variable $W(t)$ describing the increments $W(t_{i+1}) - W(t_i)$ is normally distributed with mean zero and variance $\Delta t = t_{i+1} - t_i$
- For $0 \leq s < t < u < v \leq T$, the increments $W(t) - W(s)$ and $W(v) - W(u)$ are statistically independent. This means that $W(t_{i+1})$ can not be determined based on its previous values, $W(t), t < i + 1$.

As the Random variable $W(t)$ is normally distributed, the probability density of the increment $W(t_{i+1}) - W(t_i) = \Delta W$ is

$$P(\Delta W) = \frac{1}{\sqrt{2\pi\Delta t}} e^{-(\Delta W)^2/2\Delta t}. \tag{2.2}$$

It should be noted that the results of the SDE are then also normally distributed.

An important aspect of the Wiener process and vital for Stochastic differential equations is the concept of sample paths. A sample path is a particular realization of each of the increments of the random variable $W(t)$. Three sample paths with different Δt are shown in figure 2.1. As listed in the second condition above, the random variable has a variance of Δt. This means that the resulting sample paths fluctuate on every timescale, as the increments scale with Δt. This is shown in figures 2.2a and 2.2b. Looking at one sequence of random variables, independent of what time steps one uses for calculation, the resulting distribution of random steps is always $\in \sigma(0, \Delta t)$. Based on the statistical independence of the increments of $W(t)$, the values change randomly, and therefore the random paths are not differentiable.

With the noise term defined, we can now look at how to calculate a stochastic integral.

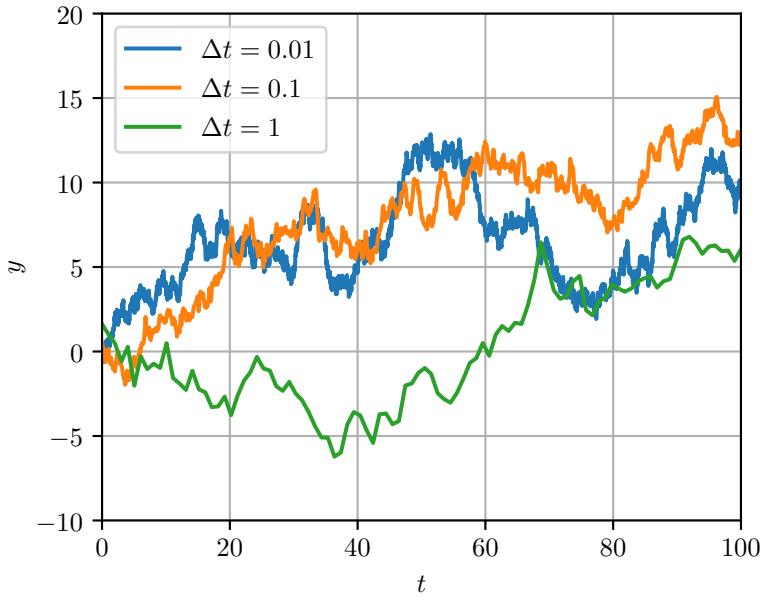

Figure 2.1: Sample paths of a Wiener process for different Δt

2.1.2 Stochastic Integral

Approximating an integral by Riemann sum, we consider the following form [5, 7]

$$\int_{t_0}^{t} G(t')dW(t') = \lim_{N\to\infty} \sum_{j=0}^{N-1} G(t_j)(W(t_{j+1}) - W(t_j)) \tag{2.3}$$

which can be interpreted as the integral of a function $G(t)$ being multiplied with the small changes made in the Brownian motion. This is the definition of the Ito integral. Another often used definition is the Stratonovich integral, with its main difference lying in where the function to be integrated is evaluated [7],

$$\int_{t_0}^{t} S(t')dW(t') = \lim_{N\to\infty} \sum_{j=0}^{N-1} S\left(\frac{t_j + t_{j+1}}{2}\right)(W(t_{j+1}) - W(t_j)). \tag{2.4}$$

The consequences of this different calculation are described in the following section.

2.1.3 Ito Stochastic Differential Equation

Following the definition of the Ito Integral, the Ito SDE is presented in the following. A stochastic quantity $x(t)$ obeys an Ito SDE, written as [9]

$$dx(t) = A[x(t), t]dt + B[x(t), t]dW(t), \tag{2.5}$$

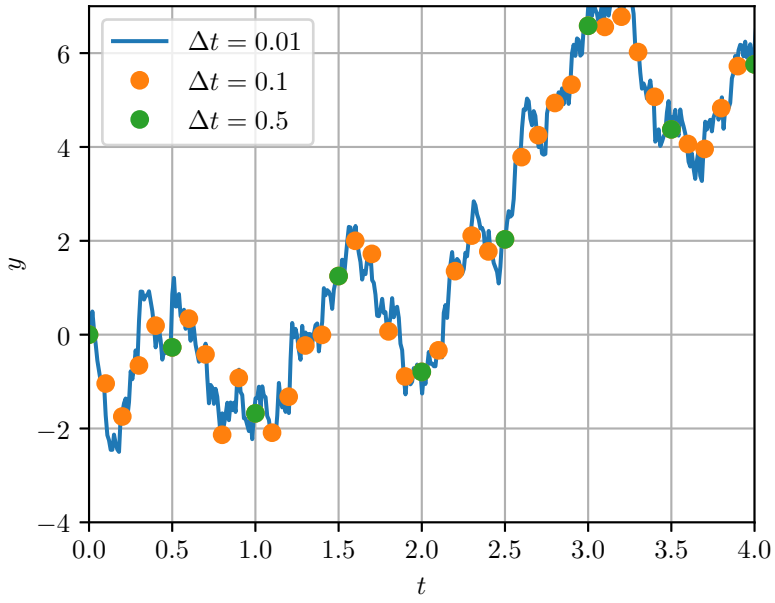

(a) Random Path of $\Delta t = 0.01$.

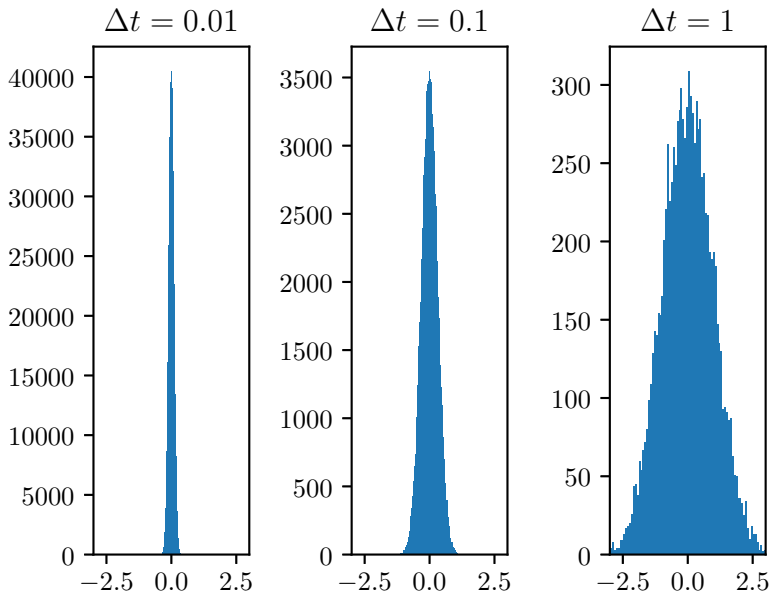

(b) Resulting distribution of increments based on the random paths of figure 2.2a

Figure 2.2: Random Path with $\Delta t = 0.01$ and the resulting distribution of increments. The standard deviations are [0.09983, 0.3166, 0.9882] which in fact equal the introduced definition of $\sqrt{\Delta t}$=[0.1, 0.316, 1].

where $A(x,t)$ and $B(x,t)$ are dependent on position and time, if for all t and $t_0 = t(0)$

$$x(t) = x(t_0) + \int_{t_0}^{t} A[x(t'),t']dt' + \int_{t_0}^{t} B[x(t'),t']dW(t'). \tag{2.6}$$

An alternative to the Ito SDE is the Stratonovich SDE which is based on the previously presented Stratonovich integral. As already shown, its main difference is the definition of where the function is evaluated. The consequences are most importantly that the Stratonovich integral is no Martingale, which is taken into account to preserve the standard chain rule for the respective SDE. Therefore, the decision on what to use often reduces on what SDE has the more convenient mathematical properties for the given task. Practically, both SDEs can be transformed into each other with identical solutions.

In the next section, we will introduce the Fokker-Planck equation, which describes the time evolution of the probability density function.

2.1.4 Fokker-Planck Equation

So far, by solving an SDE, a probability density function of the stochastic process is obtained based on Monte Carlo simulation. A large number of random paths allows the approximation of the probability density function. An alternative method is to derive a partial differential equation based on the SDE and solve it.
The Fokker-Planck equation describes the time evolution of the probability density function for stochastic processes being driven by Gaussian noise. In one dimension, the Fokker-Planck equation takes the form [5]

$$\frac{\partial f(x,t)}{\partial t} = -\frac{\partial}{\partial x}[A(x,t)f(x,t)] + \frac{1}{2}\frac{\partial^2}{\partial x^2}[B(x,t)f(x,t)]. \tag{2.7}$$

where $f(x,t)$ is the probability density function.
Its solution is equivalent to the solution of the Ito SDE

$$dx(t) = A[x(t),t]dt + \sqrt{B[x(t),t]}dW(t). \tag{2.8}$$

A mayor disadvantage of presenting the process in this form in contrast to an SDE is the lack of direct information. A SDE allows for computing individual paths, whereas the Fokker-Planck equation does not.

The Fokker-Planck equation is rather used to calculate steady-state probability densities or, depending on the complexity, obtain the time evolution of the probability density function.

The next section presents numerical methods that are used to solve stochastic differential equations.

2.2 Numerical Methods to Solve SDEs

To apply numerical methods, discretization has to be done. Looking at the time interval $[0, T]$, let the time step $\Delta t = T/N$ with N being the amount of steps. That leads to $\tau_j = j\Delta t$. The numerical approximation of $X(\tau_j)$ will be noted as X_j. The noise increments are generally calculated with $W(\tau_j) - W(\tau_{j-1})$.
Before presenting numerical methods to solve SDEs, metrics to compare the different methods are shown [7].

Strong order of convergence
A method is said to have strong order of convergence of order γ, if a constant C exists such that

$$\mathbb{E}|X_n - X(\tau)| \leq C\Delta t^{\gamma} \tag{2.9}$$

for any fixed $\tau = n\Delta t \in [0, T]$ and Δt sufficiently small. $\mathbb{E}$ stands for the expected value

$$\mathbb{E} = \sum_{i=1}^{\infty} x_i p_i. \tag{2.10}$$

In words, the above expression measures the rate of decay of the mean of the errors.

Weak order of convergence
A method is said to have weak order of convergence of order γ, if a constant C exists such that for all functions p

$$|\mathbb{E}p(X_n) - \mathbb{E}p(X(\tau))| \leq C\Delta t^{\gamma} \tag{2.11}$$

for any fixed $\tau = n\Delta t \in [0, T]$ and Δt sufficiently small.
In words, the above expression measures the rate of decay of the error of the means.

Summarizing, weak convergence approximates the solution of the SDE in distribution, and the strong convergence approximates the solution of the SDE in the mean-square sense. Usually, the weak order of convergence is higher than the strong order of convergence, resulting in a higher importance of the strong order of convergence. In the following, we introduce three selected numerical methods in the order of their accuracy, starting with the simplest but also most inaccurate one, the Euler-Maruyama method.

2.2.1 Euler-Maruyama Method

The most basic approach is the Euler-Maruyama method. Discretising the SDE, the following form can be noted [7]:

$$X_j = X_{j-1} + A(X_{j-1})\Delta t + B(X_{j-1})(W(\tau_j) - W(\tau_{j-1})) \tag{2.12}$$

Consider that setting the function $B = 0$ results in the well known Euler method. Investigating the convergence of the Euler Maruyama method, a strong order of convergence with $\gamma = 1/2$ and a weak order of convergence $\gamma = 1$ can be noted.

2.2.2 Improved Euler Method

A possibility to improve the Convergence of the Euler-Maruyama method is the use of the Milstein method - or improved Euler method. Its main point is to raise the strong order of convergence by adding a correction term to the function multiplied with the noise increment [7].

$$\begin{aligned} X_j = X_{j-1} + A(X_{j-1})\Delta t + B(X_{j-1})(W(\tau_j) - W(\tau_{j-1})) \\ + \frac{1}{2}B(X_{j-1})B'(X_{j-1})((W(\tau_j) - W(\tau_{j-1}))^2 - \Delta t) \end{aligned} \tag{2.13}$$

This leads to a strong order of convergence of 1.

2.2.3 Runge Kutta 2nd Order

The last numerical methods to be listed here are the Runge Kutta like methods. As in the case of ordinary differential equations, there is a wide range possible implementations known, most notably varying in their complexity and computation cost [18]. We will keep it simple by looking at a second order Runge Kutta scheme:

$$K_1 = A(t_{j-1}, X_{j-1})\Delta t + B(t_{j-1}, X_{j-1})(\Delta W - S_k\sqrt{\Delta t}) \tag{2.14}$$

$$K_2 = A(t_j, X_{j-1} + K_1)\Delta t + B(t_j, X_{j-1} + K_1)(\Delta W + S_k\sqrt{\Delta t}) \tag{2.15}$$

$$X_j = X_{j-1} + \frac{1}{2}(K_1 + K_2) \tag{2.16}$$

where $\Delta W = W(\tau_j) - W(\tau_{j-1})$ and $S_k = \pm 1$ each with a probability of 0.5. This method results in a strong and weak convergence of one [15].

We have now investigated what stochastic differential equations are and how to solve them. In the following, we will focus on the characteristics of the structures we want to apply this theory on.

2.3 Bistable Systems

As we investigate bistable MEMS plates, we will look at the properties of such bistable systems. The Duffing oscillator will hand as an example for the following sections. It is described by [14]:

$$\ddot{x} + d\dot{x} + \omega^2 x + \beta x^3 = f sin(\omega t) + D\xi(t), \quad \langle \xi(t), \xi(s) \rangle = \delta(t - s) \tag{2.17}$$

with x as the position, $f\sin(\omega t)$ as an external force, the noise intensity D and the noise term $\xi(t)$. A common approach to analyse the oscillator is to investigate its potential. We define the potential $V(x)$ as

$$\frac{\partial V}{\partial x} = -\omega^2 x - \beta x^3 \tag{2.18}$$

The duffing oscillator itself is not a bistable system automatically, its bistability is dependent on the parameters ω and β. As shown in figure 2.3, the system is bistable for $\omega > 1$ and $\beta < 0$. The potential shows two wells - which results in the name double-well potential. Without any external force or noise, the system is always in one of these wells. If the noise intensity or the external force get high enough, the system can jump from one well to the other. A term often used in this context is the stochastic resonance, which will be explained in the next section.

2.3.1 Stochastic Resonance

Consider a bistable system driven by a weak periodic force of frequency f. The amplitude of the external driving force is so small that there is no cross-well motion. When noise is added to the system, then at an appropriate noise intensity, a periodic switching between the two wells takes place. This noise-induced phenomenon is called stochastic resonance [14].
In figure 2.4, time series of the Duffing oscillator for different noise intensities are shown. For the first picture, the noise intensity is still too low and therefore does not lead to well switching. However, in the second figure, the noise intensity is high enough and therefore leads to periodic switching between the wells.

Additional metrics to describe bistable systems are the mean first passage time and the Kramer's escape rate. They are described in the following sections.

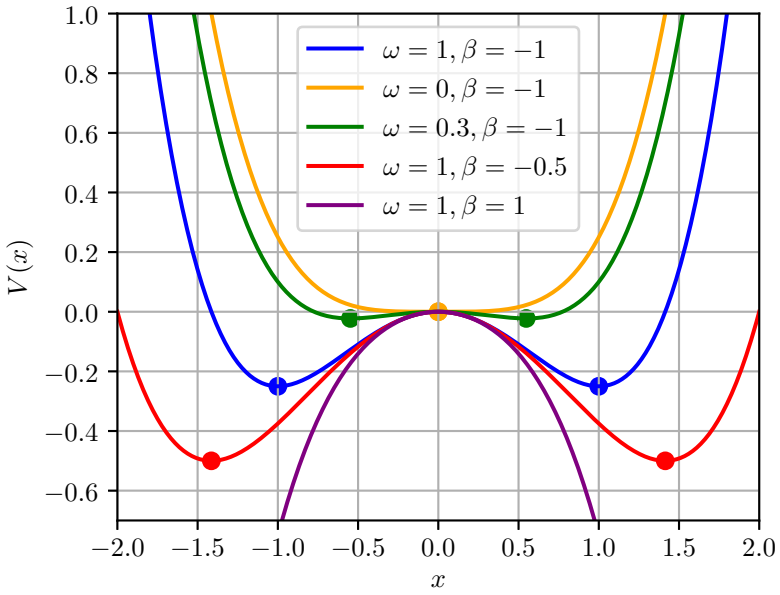

Figure 2.3: Double Well potential of duffing oscillator for varying ω and β with the potential function $V(x) = -\frac{\omega x^2}{2} - \frac{\beta x^4}{4}$.

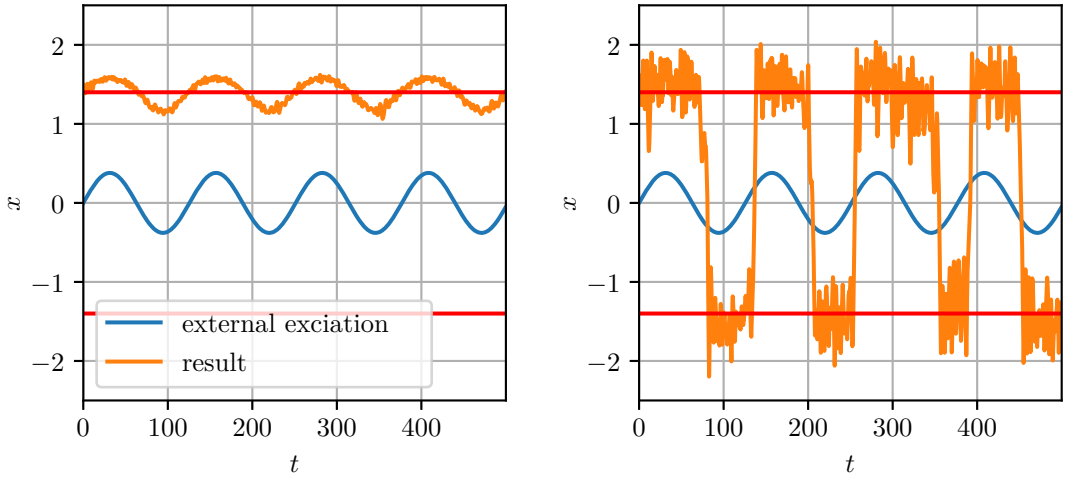

(a) $D = 0.1$ (b) $D = 0.5$

Figure 2.4: Time series of Duffing oscillator for different noise intensities. Stochastic resonance is visible for higher noise intensities (D). The red lines indicate the well minima found in the respective potential. Used parameters: $\omega = 1$, $\beta = -0.5$.

2.3.2 Mean First Passage Time

The definition of the first-passage time varies in literature, the interpretations include:

- The first time a sample path reaches a specific value
- For a particle to leave a given region
- Reaching one of the ends of a given interval

Based on the Fokker-Planck equation and its unknown probability density function f, the listed meanings can be noted mathematically.

Noting the corresponding Fokker-Planck equation of the stochastic differential equation of the Duffing oscillator

$$\partial_t p(x,t) = \partial_x[U'(x)p(x,t)] + D\partial_x^2 p(x,t) \tag{2.19}$$

with $U'(x)$ as the double well potential $U(x) = \frac{1}{2}\omega_0^2 x^2 + \frac{1}{4}\beta x^4$.

Taking the first interpretation, we define the first passage time as

$$\tau_M = \inf\{t > 0, X_t > M, x_0\} \tag{2.20}$$

with M as the boarder the process should pass and x_0 as the initial condition. The result τ_M is a stochastic process by itself, fully defined by X.

The result can now be obtained by solving the Fokker-Planck equation:

$$\int_{-\infty}^{M} p(x,t|x_0,0)dx \tag{2.21}$$

This is the probability that the particle is still in the domain after the time t. The searched result is then calculated by taking the opposite in respect to time.

2.3.3 Kramer's Escape Rate

In general, the Kramers escape rate is the characteristic escape rate from a stable state of the potential without any external added force apart from noise.
So when the external force of the Duffing oscillator $f = 0$, Kramer's time is given by the mean first passage time.

There are various approximations available, with one of them described in the

following [6]: For 1D homogenous processes, a theoretical result for the mean first passage time is

$$\mathbb{E}[\tau_m] = \frac{1}{D}\int_{-1}^{M} dx e^{V(x)/D}\int_{-\infty}^{x} e^{-V(y)/D}dy. \tag{2.22}$$

In the small noise limit $D \to 0$, a saddle-point approximation can be done: $V(y)$ is at its minimum at y_0, which means that the first derivation in the Taylor approximation can be left out. The resulting Gaussian integral can then be evaluated. This yields the Eyring-Kramers formula

$$\mathbb{E}[\tau_M] \approx \frac{2\pi}{\sqrt{|V''(0)V''(-1)|}} e^{\Delta V/D} \tag{2.23}$$

with the barrier height ΔV in the exponent divided by the noise intensity D, which is often modelled as the thermal energy $k_B T$. The Kramers rate r is now obtained by the inverse of the above term

$$r \approx \frac{1}{2\pi}\sqrt{|V''(0)V''(-1)|}\ e^{-\Delta V/D} \tag{2.24}$$

Concluding the theoretical basics, we introduced stochastic differential equations, described Brownian motion, presented numerical methods and described bistable systems. In the next chapter, we examine the model we use to describe the dynamic plate behaviour and introduce stochastic terms to model noise in the system.

Chapter 3

Model

Our model to describe the dynamic plate behaviour is based on [3, 13]. Thin rectangular microplates of planar dimensions L_x and L_y with a width h are described by using the von Karman's Plate theory based on the Kirchhoff hypothesis. Furthermore, the plate is clamped along its edges to the rest of the silicon wafer. The following assumptions are made:

- The plate is made of isotropic material
- The plate is made of homogeneous linear elastic material
- In-plane displacements in x and y are neglected
- Initial pre-stress and piezo-stress are constant over the whole plate
- Shear components of stresses are zero

3.1 Galerkin Method on the von Karman Plate Equation

The von Karman plate model resulting of above assumptions

$$\mu w'' + \mu\kappa w' + D\nabla^4 w - (N_{xx}w_{,xx} + N_{yy}w_{,yy} + 2N_{xy}w_{,xy}) = 0 \tag{3.1}$$

with w as the plate defection, the areal mass density $\mu = \rho h$, the damping rate κ and the flexure rigidity D. The prime indicates differentiation in respect to time, and the comma differentiation with respect to the spatial coordinates after the comma. The in-plane stresses N can be decomposed into

$$N_\mu(t,x,y) = N_\mu^{(b)}(t,x,y) + N_\mu^{(0)}(x,y) + N_\mu^{(p)}(t,x,y), \quad \mu \in \{xx, yy, zz\} \tag{3.2}$$

with the stress resulting of the bending stress $N^{(b)}$, pre stress $N^{(0)}$ and the piezo stress $N^{(p)}$. Stress resultants are calculated as

$$N_\mu(t,x,y) = \int_{-h/2}^{h/2} \sigma_\mu(t,x,y,z)dz, \quad \mu \in \{xx, yy, zz\}. \tag{3.3}$$

We introduce a Airy stress function defined as

$$F_{,xx} = N_{yy}, \quad F_{,yy} = N_{xx}, \quad F_{,xy} = -N_{xy}. \tag{3.4}$$

Introducing the following non-dimensional quantities

$$\begin{gathered} \bar{x} = \frac{x}{L_x}, \quad \bar{y} = \frac{y}{L_y}, \quad T = \sqrt{\frac{\mu L_x^4}{D}} \quad \bar{t} = \frac{t}{T}, \quad \bar{w} = \frac{w}{h}, \quad \bar{\kappa} = T\kappa, \\ \bar{F} = \frac{F}{D}, \quad \bar{N}_\mu^{(0)} = \frac{L_\mu^2 N_\mu^{(0)}}{D}, \quad \bar{N}_\mu^{(p)} = \frac{L_\mu^2 N_\mu^{(p)}(T\bar{t})}{D}, \quad \bar{\Theta} = \frac{\Theta}{D} \end{gathered} \tag{3.5}$$

with the temperature Θ results in the equation system

$$\ddot{\bar{w}} + \bar{\kappa}\dot{\bar{w}} + \bar{\nabla}^4\bar{w} - \left(\frac{L_x}{L_y}\right)^2 (\bar{F}_{,\bar{y}\bar{y}}\bar{w}_{,\bar{x}\bar{x}} + \bar{F}_{,\bar{x}\bar{x}}\bar{w}_{,\bar{y}\bar{y}} - 2\bar{F}_{,\bar{x}\bar{y}}\bar{w}_{,\bar{x}\bar{y}}) = 0 \tag{3.6}$$

and the corresponding compatibility equation

$$\nabla^4 F = Eh(w_{,xy}^2 - w_{,xx}w_{,yy}) \tag{3.7}$$

with the Young's modulus E. To obtain an approximate solution, a Galerkin approach is used. Note the Einstein summation convention

$$\bar{w}(\bar{x},\bar{y},\bar{t}) \approx \sum_{j=1}^{N} q_j(t)\phi_j(x,y). \tag{3.8}$$

Using the basis functions by Murphy [12]

$$\begin{aligned} \phi_i(x,y) = &(cos\left((i_{\bar{x}} - 1)\pi\bar{x}\right) - cos\left((i_{\bar{x}} + 1)\pi\bar{x}\right)) \\ &\times (cos\left((i_{\bar{y}} - 1)\pi\bar{y}\right) - cos\left((i_{\bar{y}} + 1)\pi\bar{y}\right)) \end{aligned} \tag{3.9}$$

with

$$i_y = (i-1) \bmod(\sqrt{N}), \quad i_x = \left\lfloor \frac{i-1}{\sqrt{N}} \right\rfloor \tag{3.10}$$

using the Floor function $\lfloor\cdot\rfloor$, $N \in [2, 4, 16, ..]$ and $i \in [1, ..N]$.

That leads to the final equation system

$$M_{ij}\ddot{q}_j + \frac{\bar{\kappa}}{\mu}M_{ij}\dot{q}_j + K_{ij}q_j + \left(\bar{N}^{(0)} + \bar{N}^{(p)}(t)\right)C_{ij}q_j + G_{ijkl}q_jq_kq_l = 0. \tag{3.11}$$

The needed coefficients are listed in SDE Coefficients.
As will be described later, for the most part of this thesis only the first four modes are used. This results in a simplified equation system.

3.2 Building the SDE – Studying the Impact of Temperature

Having obtained the system of differential equations describing the dynamic behaviour of the plate, the influence of noise - the force noise, can now be studied. Our first step is to model the temperature induced noise on the structure. We do this by including an additive noise term $F_{\text{noise}}(\mathbf{x})$,

$$\ddot{\bar{w}} + \frac{\bar{\kappa}}{\mu}\dot{\bar{w}} + \bar{\nabla}^4\bar{w} - \left(\frac{L_x}{L_y}\right)^2 (\bar{F}_{,\bar{y}\bar{y}}\bar{w}_{,\bar{x}\bar{x}} + \bar{F}_{,\bar{x}\bar{x}}\bar{w}_{,\bar{y}\bar{y}} - 2\bar{F}_{,\bar{x}\bar{y}}\bar{w}_{,\bar{x}\bar{y}}) = F_{\text{noise}}(\mathbf{x}, t). \quad (3.12)$$

Applying the Galerkin Method as presented in section 3.1, the following short notation is used:

$$\int F_{\text{noise}}(\mathbf{x})\phi_i(\mathbf{x}) = \hat{F}_i. \quad (3.13)$$

This results in the final equation system

$$M_{ii}\ddot{q}_i + \frac{\bar{\kappa}}{\mu}M_{ii}\dot{q}_i + \nabla V_i(\mathbf{q}) = \hat{F}_i. \quad (3.14)$$

with the potential gradient

$$\nabla V_i(\mathbf{q}) = K_{ij}q_i + \left(\bar{N}^{(0)} + \bar{N}^{(p)}(t)\right) C_{ij}q_i + G_{ijkl}q_jq_kq_l. \quad (3.15)$$

The noise term is noted in the following manner, utilizing a common notation in the context of SDEs and Fokker-Planck equations [4]:

$$\hat{F}_i = \sqrt{2\bar{D}_i}\,\eta(\bar{t}) \quad (3.16)$$

While $\eta(t)$ is already introduced as $W(t)$ in section 2.1.1, the noise intensity $\bar{D}_i$ is to be defined yet.
A well known concept from classical statistical mechanics is the equipartition theorem. It gives the total average kinetic energy for a system at a given temperature. Based on this theorem, the noise intensity of the SDE has to follow a certain relationship with the temperature. For a system with one degree of freedom it is described by

$$\langle E_{\text{kin}}\rangle = \left\langle \frac{mv^2}{2} \right\rangle = \frac{1}{2}k_BT, \quad (3.17)$$

with the system's mass m, its velocity v, the Boltzmann constant k_B and the temperature T [8].

An equation with an equivalent form to equation 3.14 is the Klein-Kramers equation, which obeys the equipartition theorem (eq. 3.17) [5].

$$m\frac{d^2x}{dt^2} = -\xi m\frac{dx}{dt} - \nabla V(x) + \sqrt{2m\xi k_B T}\,\eta(t). \tag{3.18}$$

Comparing the coefficients of equations 3.14 and 3.18, the temperature (Θ) induced noise intensity of our SDE results in

$$\bar{D}_i = M_i\frac{\bar{\kappa}}{\mu}\cdot k_B\bar{\Theta} \tag{3.19}$$

This approach ensures compliance with the equipartition theorem. In the next section, we will consider noise in the piezo-layer.

3.3 Building the SDE - Noise on the Piezo

Besides the force noise we added to the stochastic differential equation, it is also possible to study noise in the form of voltage on the piezo-layer that induces stress on the plate. For now, an applied voltage is part of the potential function V_i in the form of the stress resultants. As applying noise would be an additive part, we exclude this additional part of the potential function V_i and multiply it with a new noise term η_2

$$M_i\ddot{q}_i = -M_i\frac{\bar{\kappa}}{\mu}\dot{q}_i - \nabla V_i(\mathbf{q}) + \sqrt{2M_i\frac{\bar{\kappa}}{\mu}k_B\bar{\Theta}}\cdot\eta_1(t) + \bar{N}_{\text{noise}}C_iq_i\cdot\eta_2(t). \tag{3.20}$$

N_{noise} is a scaling parameter, being multiplied with the same coefficients an applied voltage in the potential term $V_i(\mathbf{q})$ is. The appearance of a generalized coordinate q_i in the noise intensity term is an important change to the form of our SDE. As noted in the theory section (2.2) concerning numerical methods to solve SDEs, this linearity in q leads to higher inaccuracy if just the Euler-Maruyama method is applied. In contrast, the Milstein method includes an additional term leading to a higher strong convergence.

3.4 Approximations

In general, the first four modes are considered in this thesis. Due to the nature of the equations, which have a first and second derivative of the generalized coordinate

q, an 8-dimensional stochastic differential equation is obtained (**SDE1**).

$$\begin{aligned}
\dot{q_1} &= v_1 \\
\dot{q_2} &= v_2 \\
\dot{q_3} &= v_3 \\
\dot{q_4} &= v_4 \\
M_1\dot{v}_1 &= -\tfrac{\bar{\kappa}}{\mu}M_1v_1 - \nabla V_1(\mathbf{q}) + D_1\eta(t) \\
M_2\dot{v}_2 &= -\tfrac{\bar{\kappa}}{\mu}M_2v_2 - \nabla V_2(\mathbf{q}) + D_2\eta(t) \\
M_3\dot{v}_3 &= -\tfrac{\bar{\kappa}}{\mu}M_3v_3 - \nabla V_3(\mathbf{q}) + D_3\eta(t) \\
M_4\dot{v}_4 &= -\tfrac{\bar{\kappa}}{\mu}M_4v_4 - \nabla V_4(\mathbf{q}) + D_4\eta(t)
\end{aligned} \tag{3.21}$$

To simplify the notation, the noise terms introduced in the previous sections are shortened by the expressions

$$D_i\eta(t) = \sqrt{2\bar{D}_i}\,\eta_1(\bar{t}) + \bar{N}_{\text{noise}}C_iq_i \cdot \eta_2(t). \tag{3.22}$$

As described in section 2.3, we will examine the potential function of the system in the following.

3.4.1 Effective Potential

Analysing the model, we examine the potential. Since the first mode dominates, we look at the potential function V_1. As shown in Figure 3.1, the system exhibits clear bistability for pre-stresses greater than $1.0n_{cr}$, with the critical stress n_{cr} defined as

$$n_{cr} = \frac{-48\pi^4DL_x^4 - 32\pi^4DL_x^2L_y^2 - 48\pi^4DL_y^4}{12\pi^2L_x^2L_y^2(L_x^2 + L_y^2)}. \tag{3.23}$$

To induce a snap-through, the barrier between the two wells must be overcome. Although this plot helps to gain a qualitative understanding of the plate's behaviour, it is a simplification as only the first mode is considered. We will look into possible approximations in the next section.

3.4.2 Fokker-Planck Equation

Following the process presented in section 2.1.4, we obtain the corresponding Fokker-Planck equation:

$$\frac{\partial f(\mathbf{x},t)}{\partial t} = \sum_{i=1}^{N} -\frac{\partial}{\partial x_i}[A_i(\mathbf{x},t)f(\mathbf{x},t)] + \frac{1}{2}\sum_{i=1}^{N}\sum_{j=1}^{N}\frac{\partial^2}{\partial x_i\partial x_j}[B_{ij}(\mathbf{x},t)f(\mathbf{x},t)]. \tag{3.24}$$

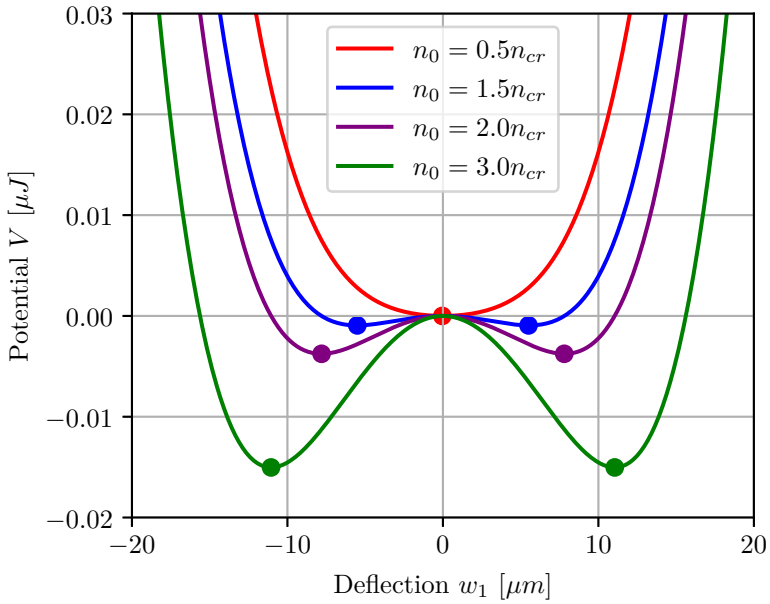

Figure 3.1: Potential function of mode 1 for different pre-stresses. Used parameters are listed in table 5.1. For the evaluation, all time derivatives are set to zero.

where $f(\mathbf{x}, t)$ is the probability density function and $\mathbf{x} = (q_1, q_2, q_3, q_4, v_1, v_2, v_3, v_4)^T$ The matrices $\mathbf{A}$ and $\mathbf{B}$ are

$$\mathbf{A}^\intercal = \begin{pmatrix} v_1 \\ v_2 \\ v_3 \\ v_4 \\ -\frac{1}{M_1}\left(\frac{\bar{\kappa}}{\mu} M_1 v_1 + \nabla V_1(\mathbf{q})\right) \\ -\frac{1}{M_2}\left(\frac{\bar{\kappa}}{\mu} M_2 v_2 + \nabla V_2(\mathbf{q})\right) \\ -\frac{1}{M_3}\left(\frac{\bar{\kappa}}{\mu} M_3 v_3 + \nabla V_3(\mathbf{q})\right) \\ -\frac{1}{M_4}\left(\frac{\bar{\kappa}}{\mu} M_4 v_4 + \nabla V_4(\mathbf{q})\right) \end{pmatrix} \tag{3.25}$$

$$\mathbf{B} = \begin{pmatrix} 0 & 0 & 0 & 0 & 0 & 0 & 0 & 0 \\ 0 & 0 & 0 & 0 & 0 & 0 & 0 & 0 \\ 0 & 0 & 0 & 0 & 0 & 0 & 0 & 0 \\ 0 & 0 & 0 & 0 & 0 & 0 & 0 & 0 \\ 0 & 0 & 0 & 0 & D_1^2/2 & 0 & 0 & 0 \\ 0 & 0 & 0 & 0 & 0 & D_2^2/2 & 0 & 0 \\ 0 & 0 & 0 & 0 & 0 & 0 & D_3^2/2 & 0 \\ 0 & 0 & 0 & 0 & 0 & 0 & 0 & D_4^2/2 \end{pmatrix}. \tag{3.26}$$

Due to the complexity of this equation ($\mathbf{x}$ has 8 dimensions), solving it for a probability density function is computationally demanding. An approach to overcome this problem is to make approximations regarding the number of modes considered. We will examine two variations:

- Approximation 1 (**SDE2**): We consider only mode 1 and disregard the impact of any other modes. This leads to a two-dimensional SDE.

$$\dot{q}_1 = v_1 \tag{3.27a}$$

$$M_{11}\dot{v}_1 = -\frac{\bar{\kappa}M_{11}}{\mu}v_1 - \frac{\partial V_1(q_1,t)}{\partial q_1} + D_1\eta_1(t) \tag{3.27b}$$

- Approximation 2 (**SDE3**): Further inspecting Approximation 1, the damping force could be greater than the inertia ($\frac{\kappa M_{11}}{\mu} > M_{11}$). As a result, dropping the first term leads to the special case of overdamped dynamics.

$$\frac{\bar{\kappa}M_{11}}{\mu}\dot{q}_1 = -\frac{\partial V(q_1,t)}{\partial q_1} + D_1\eta_1(t) \tag{3.28}$$

We will later analyse the differences in results and compare them with the ones obtained from Monte Carlo simulations.

3.5 Converting Voltages Into Stresses

An important aspect when comparing simulations with measurement results is converting voltages applied on the piezo-layer into stresses that we use in the theoretical model. The stress-change induced by applying a voltage can be calculated by

$$\Delta\sigma_{\mathrm{AlN}} = \left(\frac{1}{2}\frac{C_{13}^2}{C_{33}} - C_{11} - C_{12}\right) d_{31}E_3 \tag{3.29}$$

with $\Delta\sigma_{AlN}$ as the change of stress in the aluminium nitride (AlN) piezo-layer and E_3 as the resulting electric field along the z-axis [2]. The values of the entries of the elasticity tensor $\mathbf{C}$ and the piezoelectric coefficient d_{31} are listed in table 3.1.

Table 3.1: Mechanical and piezoelectric parameters of aluminium nitride to calculate the stress change resulting of an applied voltage [2]

C_{11}[GPa]	C_{12}[GPa]	C_{13}[GPa]	C_{33}[GPa]	d_{31}[pm V^{-1}]
410	149	99	389	−1.36

Finally, the stress resultants $N_{xx}, N_{yy}, N_{xy}, N_{noise}$ are calculated as described in equation 3.3. This leads to the following final equation to calculate the stress resultants

$$N_{noise} = U_p \frac{h \cdot \left(\frac{1}{2}\frac{C_{13}^2}{C_{33}} - C_{11} - C_{12}\right) d_{31}}{h_{AlN}} \tag{3.30}$$

with the thickness of the AlN layer h_{AlN} and the thickness of the plate h.

In this chapter, we described the used model and added stochastic terms. Furthermore, we introduced approximations which could ease solving the Fokker-Planck equation. Finally, we investigated the connection between induced stresses and applied voltage. In the next chapter, the framework built in context of this thesis will be presented.

Chapter 4

Implementation

The framework utilized in this thesis is implemented in C. The following sections will present the general structure, important code snippets and finally the scope of implemented functions.

4.1 Structure

Figure 4.1 illustrates the primary structure of the implemented code. The first step is to initialize the structures. These include the model (listing 4.1) which implements parameters describing the geometries of the structure under investigation as well as the properties of its materials. The second structure is responsible for describing the simulation (listing 4.2). In addition to the starting and ending times of the simulation, it also includes the step size, the initialization vector and the method used to solve the SDE. The final structure encompasses the excitation signal parameters (listing 4.3).

The subsequent step involves executing the solver. After initializing the values, the next step is calculated by executing the chosen method. Afterwards, the results are saved and, if necessary, used to update the values for the next step. Once all desired steps are done, the values are saved in a file.

This concludes the description of the general structure of the solver. In the next section, important code snippets will be presented.

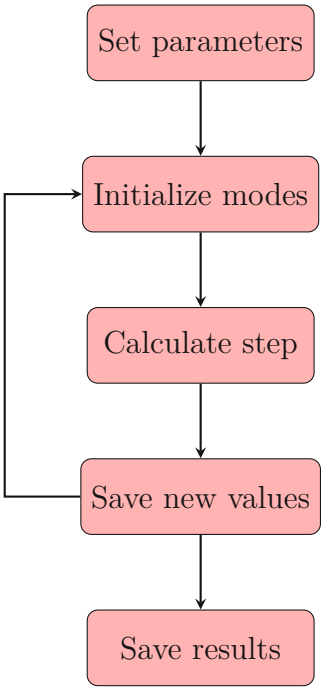

Figure 4.1: Flow Chart showing the code structure

```
struct param_mod {
    double Lx;
    double Ly;
    double E;
    double h;
    double nu_num;
    double n_cr;
    double kappa;
    double mu;
    double M[4];
    double C[8];
    double K[4];
    double G[17];
    double D;
    double sigma_max[4];
    double T_norm;
};
```

Listing 4.1: Model Structure

```
struct param_sim {
    double t_start;
    double t_end;
    double step;
    int amount_step;
```

```
6     double init[8];
7     char path_save[40];
8     int method;
9 };
```

Listing 4.2: Simulation Structure

```
1 struct param_exc {
2     int excitation_type;
3     double n0;
4     double np0;
5     double npoffset;
6     double f;
7     double start;
8     double amount_periods;
9     double dutycycle;
10    double D_bar[4];
11    double P[4];
12    double T;
13 };
```

Listing 4.3: Excitation Structure

4.2 Important Code Snippets

As the implementation is an integral part of this thesis, we will look at some important code snippets.

4.2.1 Implementation of Algorithms

We start with the implementation of the solvers. Listing 4.4 shows the Code used to implement the Euler Maruyama scheme for the one-dimensional SDE. As shown in section 2.2, this scheme has the following form:

$$X_j = X_{j-1} + A(X_{j-1})\Delta t + B(X_{j-1})(W(\tau_j) - W(\tau_{j-1})). \tag{4.1}$$

Line 1 is used to calculate the function value based on the previous step ($A(X_{j-1})$) and line 3 shows the appliance of the Euler Maruyama method.

```
1 k1_0 = - (((K11) + (stress_term * C11)) * q1) - (G11 * pow(q1,3));
2
3 q1_new = q1 + ((k1_0 * Dt) + (S1 * W1))* 1/(kappa / mu * M1);
```

Listing 4.4: Code Snippet 1D SDE

Listing 4.5 presents the implementation of the two-dimensional SDE, again with the Euler Maruyama method. In contrast to the previous code, the two added lines are rather simple, as they are just used to sum up the velocity and therefore calculate the absolute deflection of the plate.

```
1 k1_0 = v1;
2 k1_1 = - (kappa / mu * M1 * v1) - (((K11) + (stress_term * C11)) * q1
      ) - (G11 * pow(q1,3)) ;
3 q1_new = q1 + (k1_0 * Dt);
4 v1_new = v1 + (k1_1 * Dt) + (S1 * W1);
```

Listing 4.5: Code Snippet 2D SDE

Furthermore, listing 4.6 shows the whole eight-dimensional SDE. As the full potential is calculated, a method is used to structure the code. Other than that, the code just scaled based on the previously shown snippets.

```
1 k1_0 = v1/M1;
2 k1_1 = v2/M2;
3 k1_2 = v3/M3;
4 k1_3 = v4/M4;
5 k1_4 = g_f(1, t, q1, q2, q3, q4, v1/M1, v2/M2, v3/M3, v4/M4, stress,
      s1, e1);
6 k1_5 = g_f(2, t, q1, q2, q3, q4, v1/M1, v2/M2, v3/M3, v4/M4, stress,
      s1, e1);
7 k1_6 = g_f(3, t, q1, q2, q3, q4, v1/M1, v2/M2, v3/M3, v4/M4, stress,
      s1, e1);
8 k1_7 = g_f(4, t, q1, q2, q3, q4, v1/M1, v2/M2, v3/M3, v4/M4, stress,
      s1, e1);
9
10 q1_new = q1 + (k1_0 * Dt);
11 q2_new = q2 + (k1_1 * Dt);
12 q3_new = q3 + (k1_2 * Dt);
13 q4_new = q4 + (k1_3 * Dt);
14 v1_new = v1 + (k1_4 * Dt) + (S1 * W1);
15 v2_new = v2 + (k1_5 * Dt) + (S2 * W2);
16 v3_new = v3 + (k1_6 * Dt) + (S3 * W3);
17 v4_new = v4 + (k1_7 * Dt) + (S4 * W4);
```

Listing 4.6: Code Snippet 8D SDE

Listing 4.7 highlights the implementation of the Milstein method. The most interesting is line 8, which starts with the terms already seen in the Euler implementation but adds terms to achieve the higher strong convergence, as also shown in section 2.2,

$$\begin{aligned} X_j = X_{j-1} + A(X_{j-1})\Delta t + B(X_{j-1})(W(\tau_j) - W(\tau_{j-1})) \\ + \frac{1}{2} B(X_{j-1})B'(X_{j-1})((W(\tau_j) - W(\tau_{j-1}))^2 - \Delta t). \end{aligned} \tag{4.2}$$

```
k1_0 = v1/M1;
...
k1_4 = g_f(1, stress, t, q1, q2, q3, q4, v1/M1, v2/M2, v3/M3, v4/M4,
    s1, e1);
...

q1_new = q1 + (k1_0 * Dt);
...
v1_new = v1 + (k1_4  *Dt) + (S1 * W1) + (P1 * C11 * q1 * W1) + (0.5 *
     P1 * C11 * q1 * C11 * ((W1 * W1)-Dt));
...
```

Listing 4.7: Implementation of Milstein method

Finally, we also look at the implementation of the RK2 method in listing 4.8,

$$K_1 = A(t_{j-1}, X_{j-1})\Delta t + B(t_{j-1}, X_{j-1})(\Delta W - S_k\sqrt{\Delta t}), \tag{4.3}$$

$$K_2 = A(t_j, X_{j-1} + K_1)\Delta t + B(t_j, X_{j-1} + K_1)(\Delta W + S_k\sqrt{\Delta t}), \tag{4.4}$$

$$X_j = X_{j-1} + \frac{1}{2}(K_1 + K_2). \tag{4.5}$$

```
k1_0 = v4/M1;
k1_4 = g_f(1, excit_k1, t_k1, q1, q2, q3, q4, v1/M1, v2/M2, v3/M3, v4
    /M4, s1, e1);

q1_1 = (k1_3 * Dt);
v1_1 = (k1_4 * Dt) + (D_bar[0] + (P1 * C11 * q1))*(W1-(S_k1*sqrt(Dt))
    );

k1_0 = (v4+q1_1)/M1;
k1_4 = g_f(1, excit_k2, t_k2, q1+q1_1, q2+q2_1, q3+q3_1, q4+q4_1, (v1
    +v1_1)/M1, (v2+v2_1)/M2, (v3+q3_1)/M3, (v4+q4_1)/M4, s1, e1);

q1_2 = (k1_0 * Dt);
v1_2 = (k1_4 * Dt) + (D_bar[0] + (P1 * C11 * (q1+q1_1)))*(W1+(S_k2*
    sqrt(Dt)));

q1_new = q1 + (0.5*(q1_1+q1_2));
v1_new = v1 + (0.5*(v1_1+v1_2));
```

Listing 4.8: Implementation of RK2

4.2.2 Obtaining a Time Series

For a better understanding of the code, we will examine how a time series of the plate deflection is simulated by applying a specific excitation. Listing 4.9 illustrates

the definition and initialization of the structs. Subsequently, the *get_time_series* method is invoked to manage the calculations.

This method is presented in parts in listing 4.10. First, the data vector is initialized with the parameters stored in the simulation struct. Then, for each desired time step, the corresponding excitation value is obtained, and the implemented solver (in this case the Euler Maruyama) is called. Finally, the structs and the results can be saved.

```
struct param_mod s1;
struct param_sim m1;
struct param_exc e1;

init_values_model(&s1);
init_values_sim(&m1, 0.,  400e-6, 1e-10, 0, &s1);
init_values_exc(0,1.1, 0.3, 0.,+1,5,0.5,0.000,280e3, 0., &e1, &s1);

get_time_series(&s1, &m1, &e1, 0, 1);
```

Listing 4.9: Obtaining a time series 1 - Initialisation

```
double q_old[8];
double q_new[8];

for(int i=0; i<8; i++)
{
    q_old[i] = m1->init[i];
}
...
for(int i=1; i<m1->amount_step; i++)
{
    double t = i*m1->step;
    double excit = get_excitation(t, s1, m1, e1);

    if(method==0)
    {
        step_euler(q_old, q_new, excit, t, m1->step, s1, e1, r);
    }
    ....

    for(int i=0; i<8; i++)
    {
        q_old[i] = q_new[i];
    }
    save_result(...);
}
save_exc(e1, filepath);
save_sim(m1, filepath);
```

```
28 save_model(s1, filepath);
```

Listing 4.10: Obtaining a time series 2 - *get_time_series* method

4.3 Scope of Functions

After examining the implementation of numerical methods, we will now explore the entire framework and its offerings. The implemented functions consist of:

- A straightforward solver for computing a single time series
- Verification of compliance with the equipartition theorem
- Assessment of the convergence of various solvers
- Generation of various maps to evaluate multiple time series

With the used framework presented, we can look at the results of this thesis, which will be done in the next chapter.

Chapter 5

Results

Before presenting the results of this work, we first define the parameters used for simulations. As long as not noted otherwise, the following values are used for all shown experiments [3].

Table 5.1: Used parameters and its values

Side lengths L_x, L_y	$700\,\mu\mathrm{m}$
Thickness h	$3.5\,\mu\mathrm{m}$
Poisson's ratio ν	0.22
Young's module E	$165\,\mathrm{GPa}$
Damping rate κ	$700\,\mathrm{kg\,m^{-2}\,s^{-1}}$
Density ρ	$2330\,\mathrm{kg\,m^{-3}}$

5.1 Numerical Methods

We start our investigation by examining the performance of the employed numerical methods. First, we demonstrate the convergence in absence of noise, thereby evaluating the methods' suitability for ordinary differential equations. Afterwards, we analyse stochastic differential equations for which we determine the weak and strong convergence.

5.1.1 Convergence in the Absence of Noise

To evaluate the convergence of the numerical methods employed, we calculate the snap-through time for a specific scenario. We apply a sinusoidal excitation with an amplitude of $0.3\,\mathrm{N_{cr}}$ with a frequency of $f = 280\,\mathrm{kHz}$. The initial pre-stress is

$1.1\,N_{cr}$. Figure 5.1 displays one time series, where the snap-through time is defined by the time from the start of the excitation until the first mode passing zero. In this example, the snap-through time is approximately 218 ms.

Figure 5.2a illustrates the snap-through time for different step times and solver methods. As expected, the Runge Kutta method of second order (RK2) performs much better than the Euler Maruyama method. The Milstein method is not shown in this graph, as the results would be the same as those of the Euler Maruyama method. With no noise term considered, both methods result in the same equation system (see section 3.4.2).

Figure 5.2b is based on the same values used in the left picture, with the addition of calculating the relative error to the previous step size for every shown point. This is done by

$$\text{error}_{\text{rel}} = \frac{T_{s,\text{previous}} - T_s}{T_{s,\text{previous}}}. \tag{5.1}$$

It can be observed that the error is significantly lower for the RK2 method than the Euler Maruyama method. Further analysis of solving the equation system without noise can be found in [3].

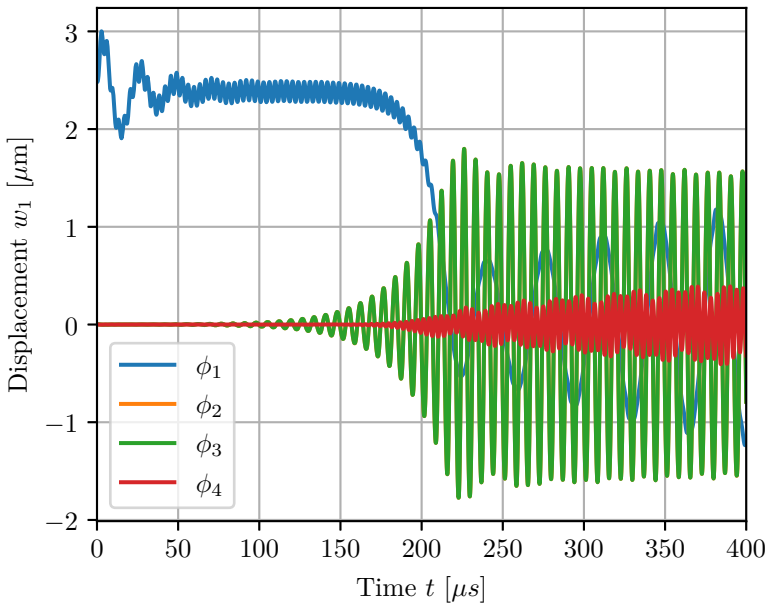

Figure 5.1: Displacement in μm. Example time series of convergence simulations. Parameters: $N_0 = 1.1\,N_{cr}$, $N_{p0} = 0.3\,N_{cr}$, $f = 280\,\text{kHz}$. Solved with Euler Maruyama method and $\Delta t = 0.1\,\text{ns}$.

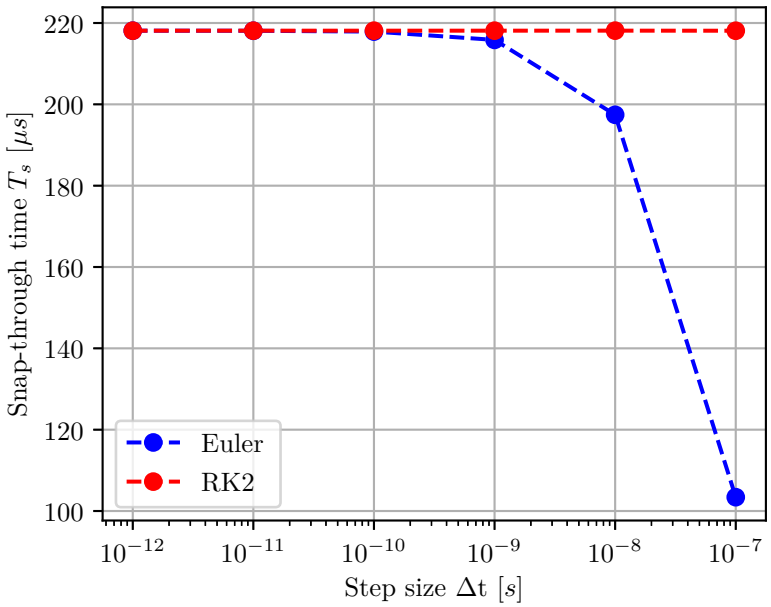

(a) Absolute Result of snap-through time.

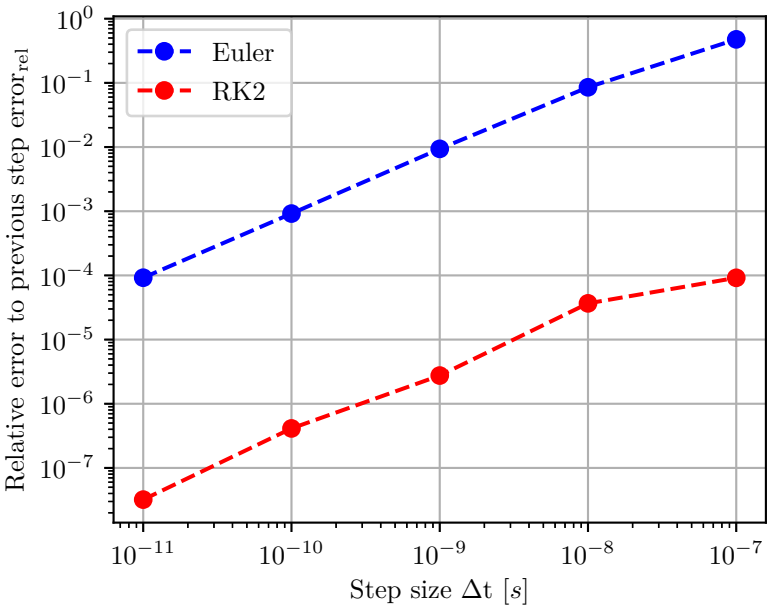

(b) Relative error of snap-through time.

Figure 5.2: Performance evaluation without considering noise. $N_0 = 1.1\,\mathrm{N_{cr}}$, $N_{p0} = 0.3\,\mathrm{N_{cr}}$, $f = 280\,\mathrm{kHz}$

After having investigated the general convergence of the equation system, our focus shifts to assessing the influence of noise.

5.1.2 Convergence in the Presence of Noise

As previously explained in theory (section 2.2), a crucial measure for assessing the performance of numerical methods in the context of stochastic differential equations is the weak and strong convergence. The lack of an analytic solution for our equation system poses a significant challenge. According to the definition of convergence metrics, such a solution would be required. However, literature suggests that it can be approximated by considering the solution of half the time step instead of the exact solution [16].

We begin with weak convergence. Since the mean of the noise is zero, regardless of the noise type, the exact mean result is approximated by using low time steps. The resulting weak convergence is then expressed as

$$|\mathbb{E}p(X_n) - \mathbb{E}p(X(\tau))| \leq C\Delta t^{\gamma} \tag{5.2}$$

with $\mathbb{E}$ as the mean value, the real value $X(\tau)$, the approximated value X_n and the weak convergence γ. This means in words that we investigate the error of the means.

The strong convergence is more complicated, as it necessitates the calculation of the errors of individual random paths. So the first step is to define the random paths, which corresponds to the seeding of the random process in programming terms. The values are not evaluated based on half the time step, but based on the lowest and therefore most accurate Δt_0. For every calculation, 10 values are summed when having a time step of $10 \cdot \Delta t$. Then the errors for every random path are computed, and their mean yields the strong convergence, as shown in the following equation

$$\mathbb{E}|X(\tau, \Delta t)) - X(\tau, \Delta t_0)| \leq C\Delta t^{\gamma}. \tag{5.3}$$

In other words, we investigate the mean of the errors.

The weak and strong convergence have been calculated for each implemented method, as illustrated below. To determine the order of convergence, the respective fitting has been performed, and the resulting values are presented in the figures. The results for the Euler Maruyama and the Milstein method align with expectations. As the mean of the noise is zero, we expected the results for the weak convergence of the Euler and Milstein method to be the same. The additional term of the Milstein method results in a higher value for the strong convergence. The errors for the calculation of weak and strong convergence of the RK2 method are

not rising for the used step sizes, which makes a fitting impossible. In comparison with the other methods, the values are much lower for higher step sizes, which is as expected. To obtain the theoretical results of the weak and strong convergence, we would need to look at a rather simple time series without highly discontinuous events like a snap-through. We still investigated this behaviour because of the importance of snap-throughs in this work.

Concluding this section examining the numerical methods, for low timesteps, RK2 performed the best for the weak convergence. Concerning the strong convergence, the Milstein method outperformed the RK2 method, which can be explained with the additional term added to the Euler Maruyama method. Looking forward to the simulations, for very small step sizes, the performance difference would not be that high. If computational time should be reduced, the RK2 method would be the method to use.

Table 5.2: Performance Evaluation of Implemented Numerical Methods

	Weak convergence	Strong convergence
Euler Maruyama	0.915	0.751
Milstein	0.915	0.915
RK2	-	-

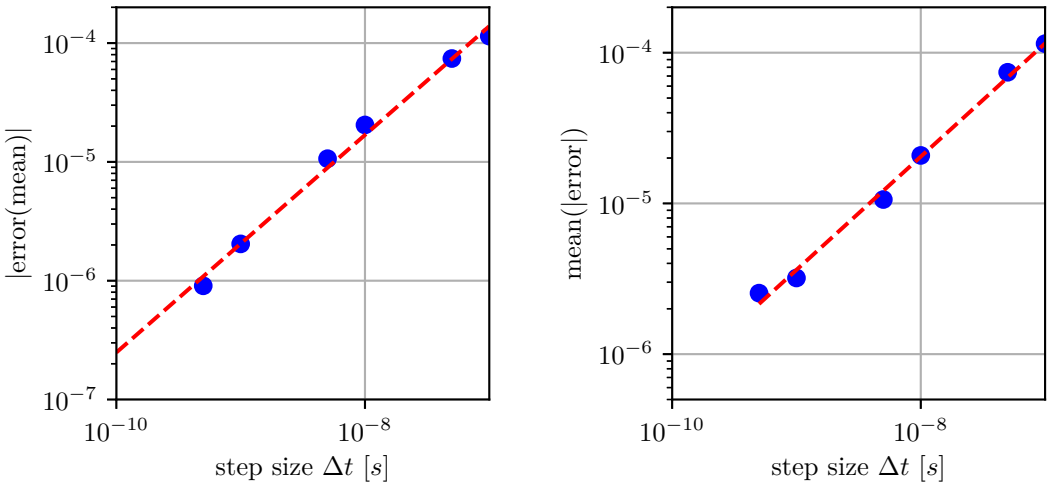

(a) Weak convergence, $\gamma = 0.915$, $C = 354.925$

(b) Strong convergence, $\gamma = 0.751$, $C = 20.978$

Figure 5.3: Convergence of Euler Maruyama method. The blue dots indicate the simulation results. The dashed red line shows the fitting of the function $C\Delta t^{\gamma}$. $N_{\text{noise}} = 0.01$, $N_{p0} = 1.1\,\text{N}_{\text{cr}}$.

5.2 Non-Excited Plate Analysis

5.2.1 Static Analysis

Besides the possibility of applying an external excitation on the plate, the pre-stress can be modified. Depending on the pre-stress, we expect the plate to behave differently. For example, for a higher pre-stress, we would expect the plate to have a higher deflection. We can investigate this behaviour by performing a static analysis. Therefore, all derivations in the equation system are set zero and the deflections are initialised with a low value to induce movement towards stable points. The results are shown in figure 5.6. Firstly, there is no stable solution other than zero before the pre-stress equals the critical stress, which is basically how the critical stress is defined. After that, the deflection of the first mode rises continuously. Modes 2 and 3 show the same behaviour because of them just being mirrored, gaining stable solutions at approximately $2.4\,\text{N}_{\text{cr}}$. Additionally, mode 4 gains stable solutions from $3.03\,\text{N}_{\text{cr}}$ onwards.

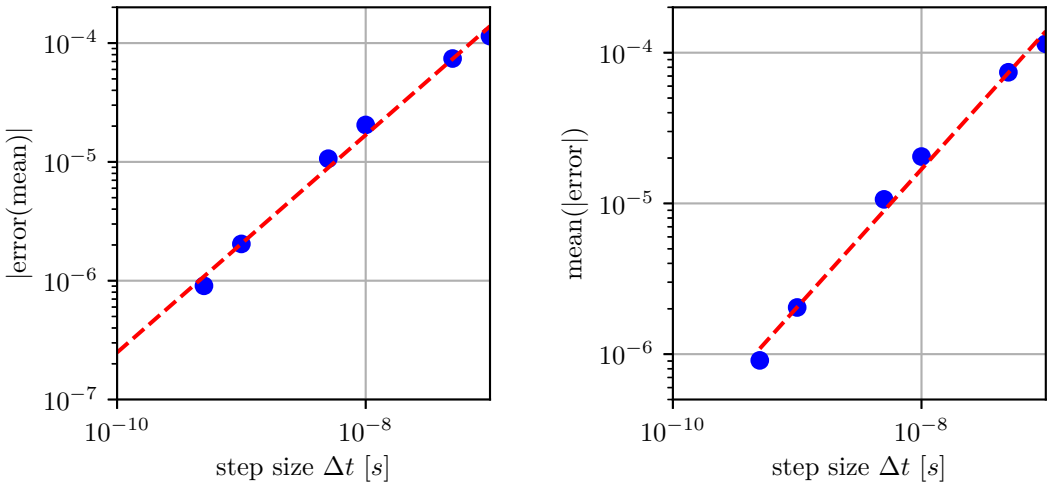

(a) Weak convergence, $\gamma = 0.915$, $C = 355.211$

(b) Strong convergence, $\gamma = 0.915$, $C = 352.642$

Figure 5.4: Convergence of Milstein method. The blue dots indicate the simulation results. The dashed red line shows the fitting of the function $C\Delta t^{\gamma}$. $N_{\text{noise}} = 0.01$, $N_{p0} = 1.1\,\text{N}_{\text{cr}}$.

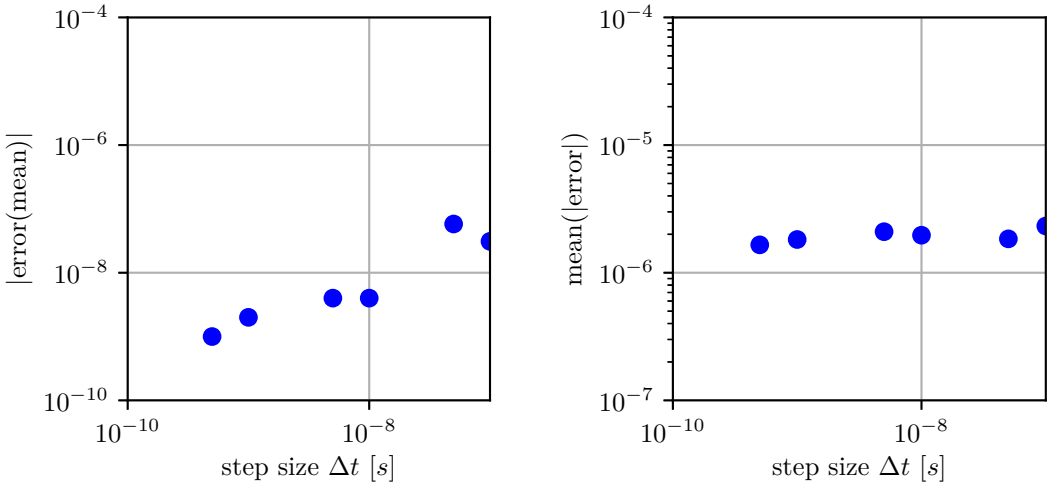

(a) Weak convergence

(b) Strong convergence

Figure 5.5: Convergence of RK2. The blue dots indicate the simulation results. $N_{\text{noise}} = 0.01$, $N_{p0} = 1.1\,\text{N}_{\text{cr}}$.

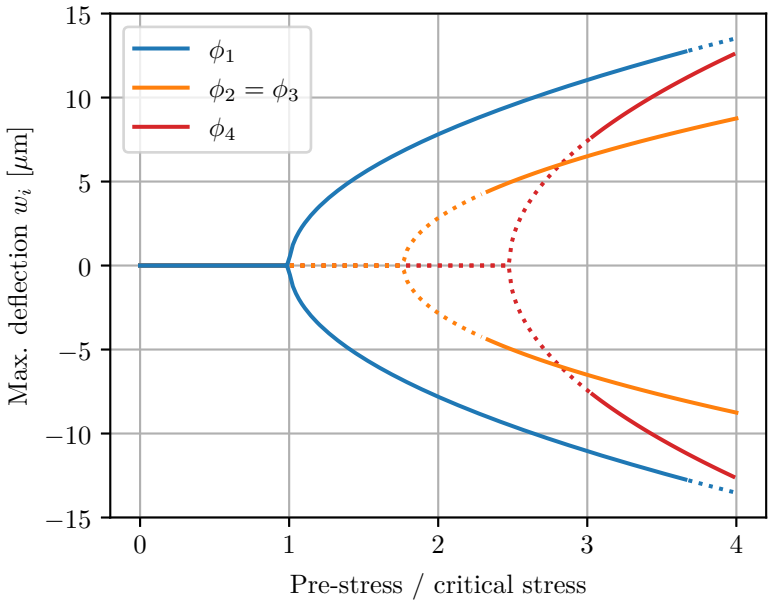

Figure 5.6: Deflection of modes versus pre-stress. Solid lines indicate stable solutions, dashed lines indicate unstable solutions.

5.2.2 Comparing Approximations With Full Model

As highlighted in section 3.4.2, solving the problem for the first four modes yields an eight-dimensional stochastic differential equation (SDE1, 3.21). To reduce computational costs, we introduced two approximations – one with two dimensions (SDE2, 3.27) and another one with one dimension (SDE3, 3.28). In this section, we compare the behaviour of the different versions, starting with a simple time series. This demonstrates the behaviour when the plate is not deflected at all, allowing us to observe the system settling into a stable state. Investigating figure 5.7, there is indeed a difference noticeable. The neglection of inertia in the one-dimensional SDE3 is evident in the lack of harmonics. Even though the result for the two-dimensional SDE2 is much more similar to the eight-dimensional SDE1, it still lacks accuracy. As the potential function of all three versions is pretty much the same (Modes two, three, and four do not play a big role for the potential of the eight-dimensional SDE), the steady-state solutions are identical.

Figure 5.8 compares the probability density functions for the deflection of the first mode after 2.8 µs obtained by solving the 2D Fokker-Planck equation [17] with the simulation results of SDE1 and SDE2. The first mode is initialized with a uniform distribution. The stable states are highlighted in every graph with the red vertical lines. The most significant difference is the higher maximum deflection observed

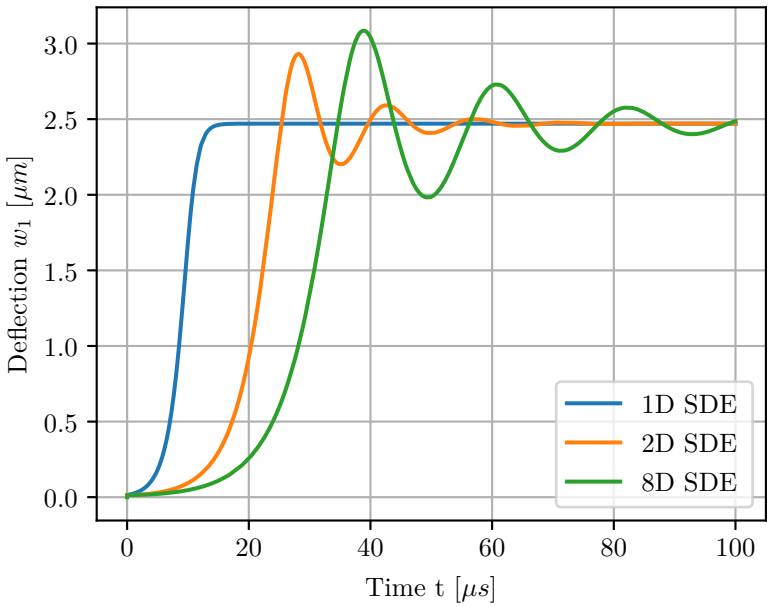

Figure 5.7: Comparison of the presented SDEs. $N_{\text{noise}} = 1.1\,\text{N}_{\text{cr}}$

for the eight-dimensional SDE1. Figure 5.10 depicts the same after 5.6 µs. An interesting difference are the second maxima at approximately −5 µm and 5 µm, which are not yet visible for the eight-dimensional SDE1. Further investigating this second maxima, we can look at the results shown in figure 5.10. For both SDEs, 50 time series are presented. In general, we can see that the observed second maxima appears because of the chosen time. Choosing 4 μs would result in opposite roles.

Finally, we investigate the same for the Fokker-Planck equation based on the one-dimensional SDE (eq. 3.28) in figures 5.11, 5.12 and 5.13. The bars represent the simulation result, while the lines show those obtained from the Fokker-Planck equation [6]. As can be seen for $t = 0$ in figure 5.11, we start with a normal distribution highlighted in blue. As expected, for later time steps, the distribution moves towards the two stable positions. Although the one-dimensional simulation results match the Fokker-Planck ones very well, the 8-dimensional SDE results (eq. 3.21) exhibit significant differences. As can be observed for $t = 0.02$, the movement towards the stable states appears much slower, which can be attributed to the neglect of mass.

Concluding this section, the results show that these approximations can work for static situations, but dealing with highly nonlinear processes such as snap-throughs, they are not accurate enough to be a real alternative.

In the next section, we will investigate the first passage time and the Cramer's

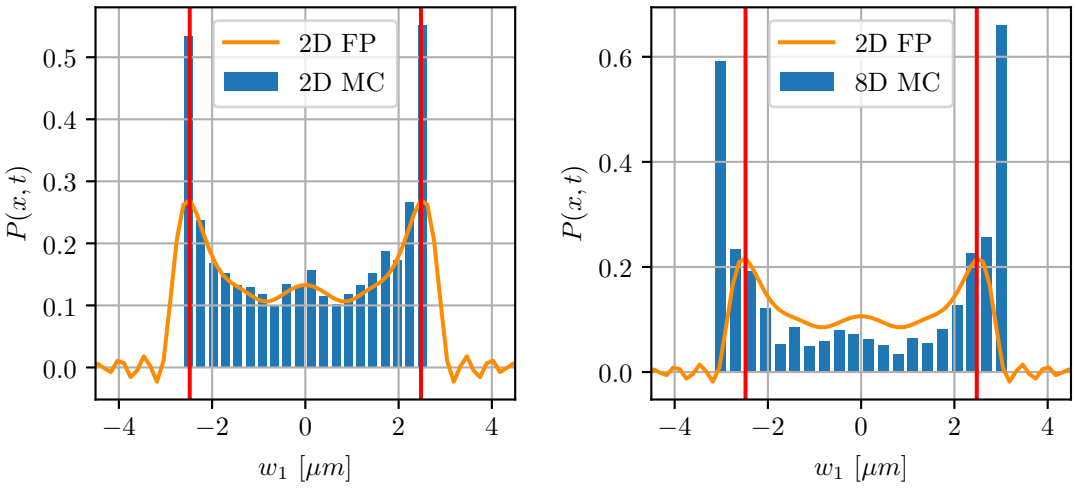

(a) 2D MC vs 2D FPE, $t = 2.8\mu s$. (b) 8D MC vs 2D FPE, $t = 2.8\mu s$.

Figure 5.8: Numerical results of Fokker-Planck equation based on 2D SDE versus 2D and 8D SDE simulation results for $t = 2.8\,\mu s$, $N_0 = 1.1\,N_{cr}$.

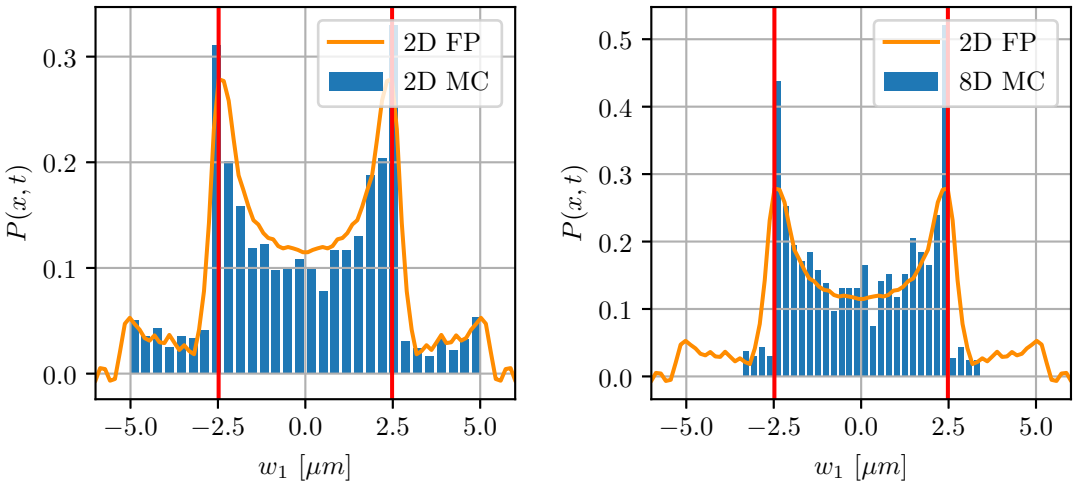

(a) 2D MC vs 2D FPE, $t = 5.6\mu s$. (b) 8D MC vs 2D FPE, $t = 5.6\mu s$.

Figure 5.9: Numerical results of Fokker-Planck equation based on 2D SDE versus 2D and 8D SDE simulation results for $t = 5.6\,\mu s$, $N_0 = 1.1\,N_{cr}$.

rate.

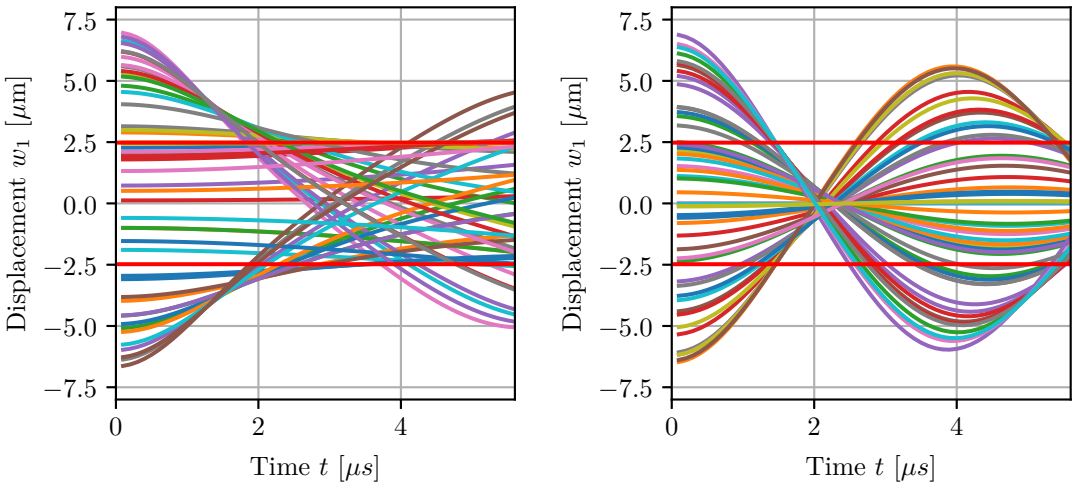

(a) 50 single time series of 2D MC, $t = 5.6\,\mu s$.

(b) 50 single time series of 8D MC, $t = 5.6\,\mu s$.

Figure 5.10: Multiple single time series of the 2D and 8D SDE for $t = 5.6\,\mu s$, $N_0 = 1.1\,N_{cr}$.

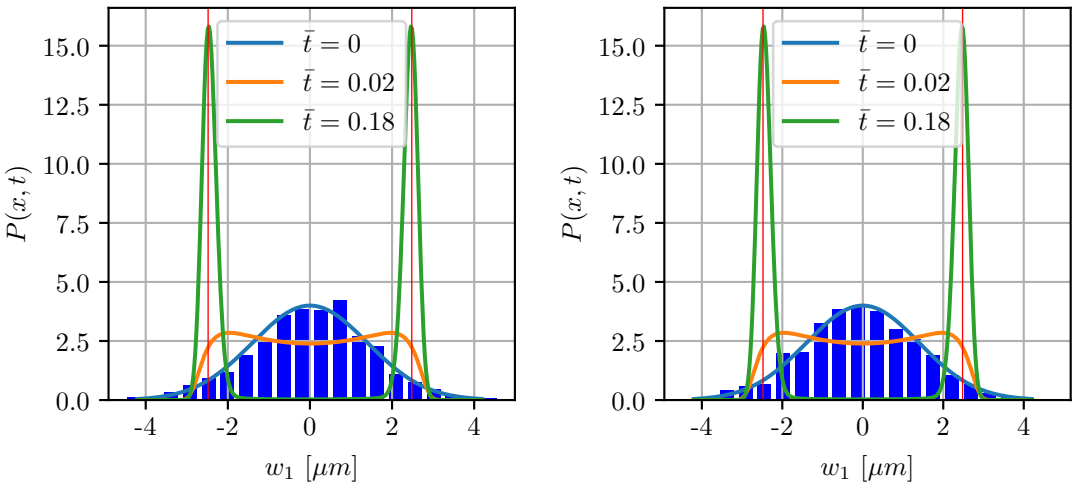

(a) 1D SDE versus 1D FPE for $\bar{t} = 0$

(b) 8D SDE versus 1D FPE for $\bar{t} = 0$

Figure 5.11: Compare Fokker-Planck result for 1D SDE (lines) with simulation results of 1D and 8D SDE (bars) for $\bar{t} = 0$, $N_0 = 1.1\,N_{cr}$.

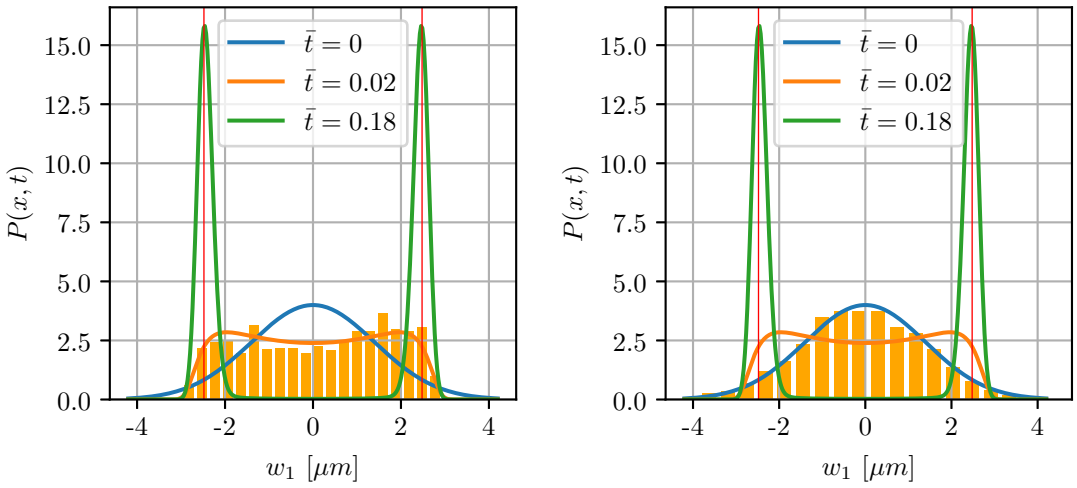

(a) 1D SDE versus 1D FPE for $\bar{t} = 0.02$ (b) 8D SDE versus 1D FPE for $\bar{t} = 0.02$

Figure 5.12: Compare Fokker-Planck result for 1D SDE (lines) with simulation results of 1D and 8D SDE (bars) for $\bar{t} = 0.02$, $N_0 = 1.1\,\mathrm{N_{cr}}$.

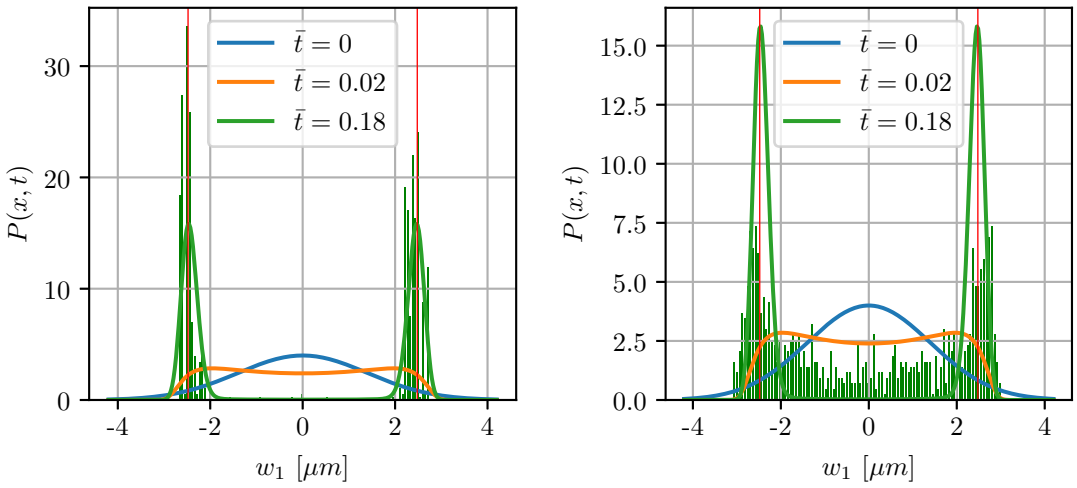

(a) 1D SDE versus 1D FPE for $\bar{t} = 0.18$ (b) 8D SDE versus 1D FPE for $\bar{t} = 0.18$

Figure 5.13: Compare Fokker-Planck result for 1D SDE (lines) with simulation results of 1D and 8D SDE (bars) for $\bar{t} = 0.18$, $N_0 = 1.1\,\mathrm{N_{cr}}$.

5.2.3 First Passage Time

To further analyse the behaviour of the plate, particularly the stochastic component of it, we examine the first passage time, which is a typical quantity used to describe

stochastic systems. Therefore, the system is initialized in a stable state. The escape rate is now defined as the probability of the system transitioning to the other stable state within one second and is calculated as shown in section 2.3.3.

$$\mathbb{E}[\tau_m] = \frac{1}{D} \int_{-1}^{M} dx e^{V(x)/D} \int_{-\infty}^{x} e^{-V(y)/D} dy. \tag{5.4}$$

The Kramers rate is calculated by

$$r \approx \frac{1}{2\pi} \sqrt{|V''(0)V''(-1)|}\ e^{-\Delta V/D}. \tag{5.5}$$

Figure 5.14 shows all the results. Firstly, the calculations are based on the one-dimensional SDE (eq. 3.28), which leads to the simulation of the one-dimensional SDE fitting the best. Secondly, as previously described in the theory, the Kramers rate is an approximation for low noise intensities. This can be observed on figure 5.14b, which shows an excellent fit for low noise intensities.

Until this point, we did not apply any excitation to the plate. We are going to change that in the next section, studying stochastic resonance.

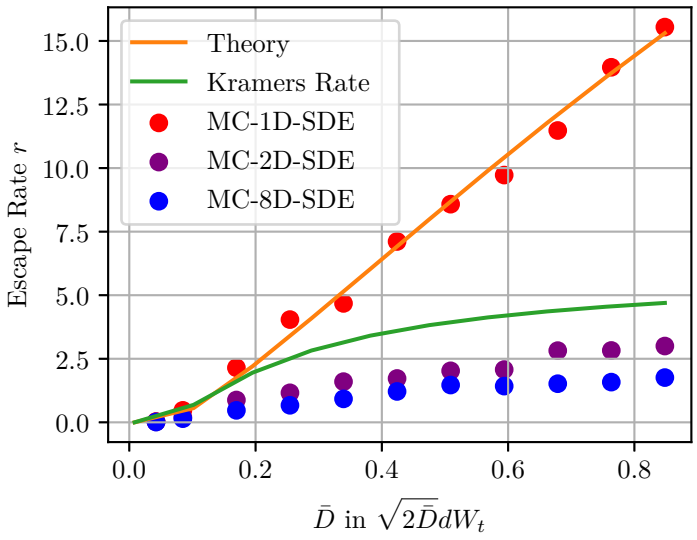

(a)

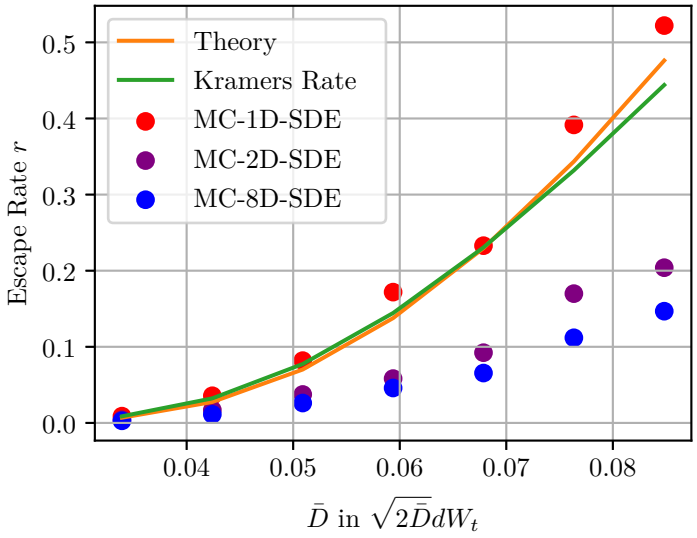

(b)

Figure 5.14: Escape Rate of theory vs Kramer's rate vs Monte Carlo Simulation. Only the temperature induced noise is considered. (b) shows the results of (a) for low noise intensities $\bar{D}$. $N_0 = 1.1\,\mathrm{N_{cr}}$.

5.3 Excited Plate Analysis - Stochastic Resonance

In this section, we investigate the stochastic resonance of our system. The first step is to visualize this phenomenon in a simple time series. To recap, we defined the stochastic resonance the following way (section 2.3): Consider a bistable system driven by a weak periodic force of frequency f. The amplitude of the external driving force is so small that there is no cross-well motion. When noise is added to the system, then at an appropriate noise intensity, a periodic switching between the two wells takes place.
This exact behaviour is shown on our system in figure 5.15. The most important realization we gain from this experiment is that the influence of the temperature induced noise is not that high. To achieve the shown switching, temperatures, much higher than ever reachable, are needed.

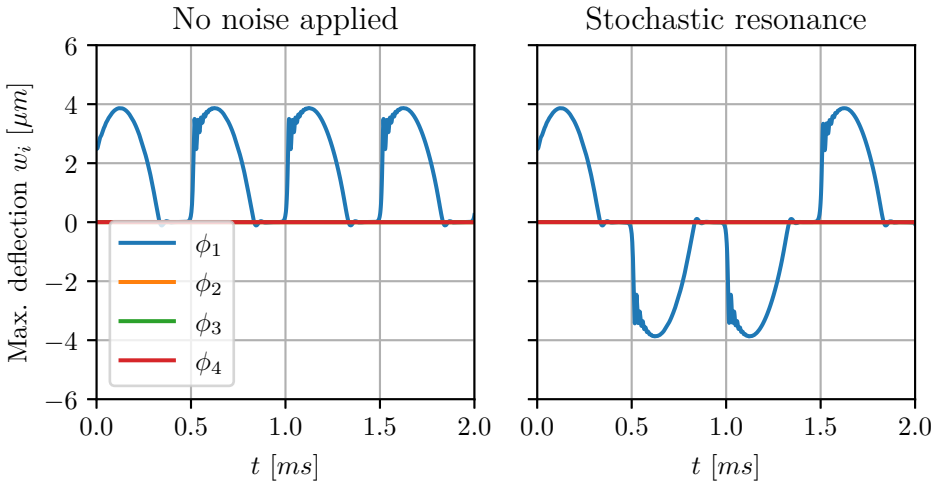

Figure 5.15: Example time series to show stochastic resonance of the plate. $N_0 = 1.1\,\mathrm{N_{cr}}$, $N_{p0} = 0.145$, 2 kHz, Temperature $\Theta = 1.5 \times 10^{10}\,\mathrm{K}$.

A term we are going to need in the following is the residency time. For the previously presented time series fig. 5.15, we can see the plate in the lower state for two periods before moving back towards the upper state, which makes the residency time two.

This single measurement can be repeated for different frequencies and figure 5.16 can be constructed [1]. The depicted data sets illustrate the number of pulses to remain in the same state successively. The likelihood indicates the probability off how many pulses the system remains in the same state after a state switch. This

has been calculated for each frequency by

$$\text{likelihood}_i = \frac{A_i}{A_{\text{total}}} \cdot 100\% \tag{5.6}$$

with A_i describing the amount of residency times of i pulses, and A_{total} as the total amount of observations made in simulation for that specific frequency. As only the mean residency times of 1 to 5 is displayed, the sum of the displayed probabilities is lower than 100%. Interestingly, for lower and higher frequencies, the mean residency time of one dominates in comparison to higher residency times. The reason for the higher frequencies is not stochastic resonance, as starting with approximately 12 kHz, the snap-throughs happen even when no noise is added. So the rise of switching action for the higher frequencies shown in the plot happens because of the excitation itself getting closer to induce a snap-through by itself. Other than that, the distributions seem quite regular. In the next section, we will

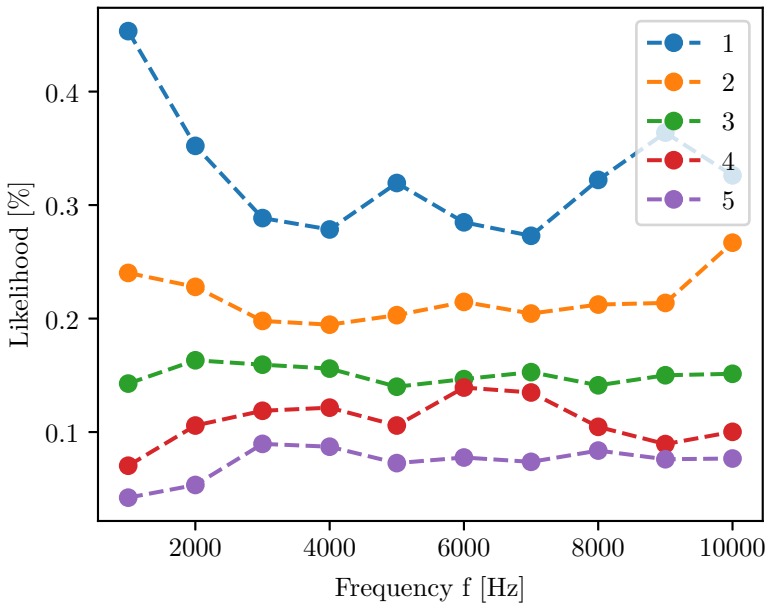

Figure 5.16: Mean Residency Time for different excitation frequencies. 500 runs per frequency, $k_B\bar{\Theta} = 1.5 \times 10^{-3}$, $N_0 = 1.1\,\mathrm{N_{cr}}$, $N_{p0} = 0.98\,\mathrm{N_{cr}}$.

further investigate the plate's behaviour under the influence of noise.

5.4 Influence of noise on the plate behaviour

In this section, we will explore the overall impact of noise on plate behaviour, particularly when combined with excitations. We will begin by examining excitation with a sine function, followed by a rectangular excitation signal, and finally, we will provide an outlook on what could be interesting to investigate in the future.

5.4.1 Sinusoidal Excitation

Beginning with the investigation of sine excitations, we utilize the signal

$$N^{(p)}(t) = N_{p0} \sin(2\pi \mathrm{ft})\, \theta(t). \tag{5.7}$$

Here, N_{p0} is the amplitude, f represents the excitation frequency and θ is the Heaviside function, that defines the start of the signal at $t = 0$. An interesting parameter of the system under this excitation is the snap-through time, which is the time it takes for the system to change its buckled state after the excitation starts. As we only investigate low pre-stresses for now, only mode one is stable. Therefore, the snap-through time T_s is defined as the time mode one deflection passes zero: $w_1(T_s) = 0$.

As shown in literature, the resulting map at $1.1\,\mathrm{N_{cr}}$ is separated into three distinct tongues (figure 5.17a)[3]. The first tongue starts to appear at an excitation amplitude $N_{p0} = 0.04\,\mathrm{N_{cr}}$ at $f = 25.5\,\mathrm{kHz}$. In comparison to the other tongues, the snap-through times are quite low, with the steps indicating that the root of this tongue lies at about 200 kHz. The other tongues appear at $N_{p0} = 0.25\,\mathrm{N_{cr}}$ and $f = 297\,\mathrm{kHz}$ and at $N_{p0} = 0.28\,\mathrm{N_{cr}}$ and $f = 489\,\mathrm{kHz}$.

After observing these results, we can add noise by considering noise in the piezo layer (as presented in section 3.3). Figure 5.17 shows the results for different noise intensities. It is important to note that these results are based on sample runs, so only show tendencies. As can be observed in 5.17b, the snap-through times for the second and third tongues decrease rapidly for still low noise intensities. Only for higher intensities (5.17c and 5.17d), the snap-through free regions are considerably impacted by the noise, and snap-throughs appear all over the place. Additionally, the first tongue's really low snap-through time segments start to crawl into the second tongue.

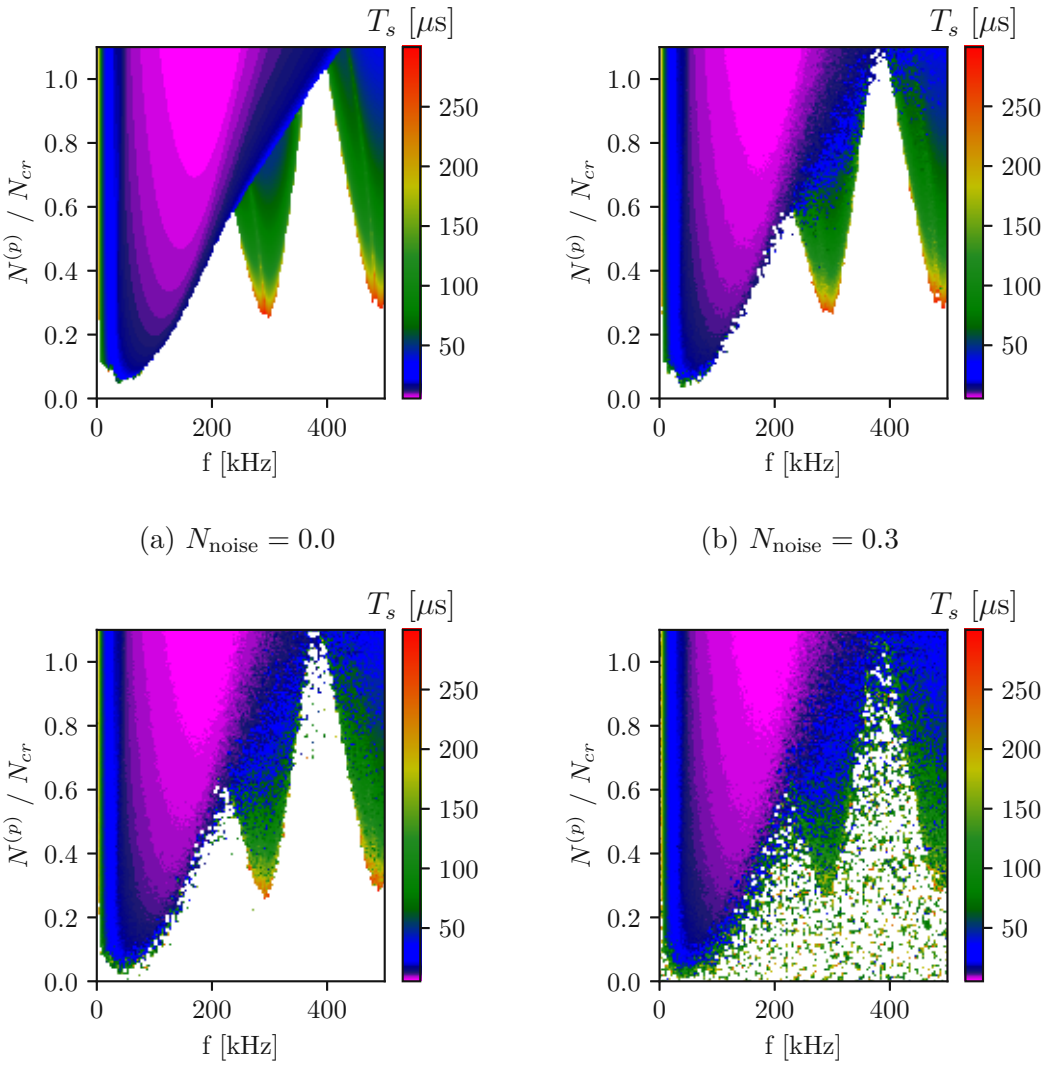

(a) $N_{\text{noise}} = 0.0$

(b) $N_{\text{noise}} = 0.3$

(c) $N_{\text{noise}} = 0.5$

(d) $N_{\text{noise}} = 0.7$

Figure 5.17: Snap-through maps for sinusoidal excitation and different noise intensities. $N_0 = 1.1\,\mathrm{N_{cr}}$.

To investigate how the influence of noise changes for different pre-stresses, we applied the same sine excitation signals while varying the pre-stress from $1.1\,\mathrm{N_{cr}}$ up to $3.5\,\mathrm{N_{cr}}$. We still keep the simplification of only considering mode 1 for the snap-through time. We can observe in figure 5.18 that the influence of noise on the areas that were snap-through free beforehand are getting less changed for higher pre-stresses.

We can explain this by thinking about the stress term. As the modelled noise intensity is independent of the pre-stress but an absolute value, the share of the noise on the resulting stress gets lower with higher pre-stress. This means that, at least for how we modelled the noise, the plate gets more robust against noise for higher pre-stresses.

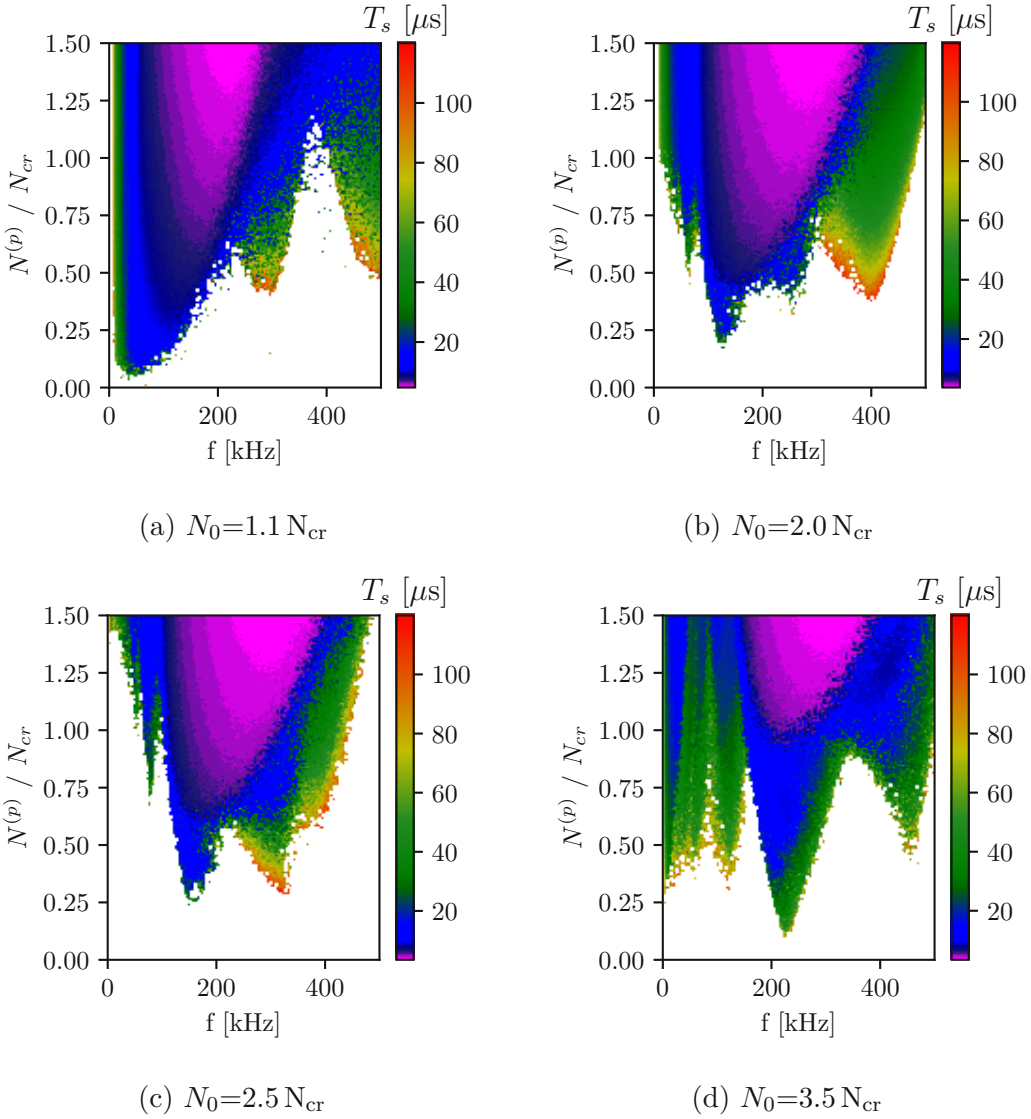

(a) N_0=1.1 N_{cr} (b) N_0=2.0 N_{cr}

(c) N_0=2.5 N_{cr} (d) N_0=3.5 N_{cr}

Figure 5.18: Snap-through times for different pre-stresses. $N_{noise} = 0.6$.

5.4.2 Rectangular Excitation

Another interesting excitation form is the rectangular signal. In contrast to sinusoidal excitations, a rectangular signal or pulses are a more intuitive approach concerning lab measurements and real applications. Additionally, first measurements of rectangular excitation of plates have already been published [2]. We define this excitation as

$$N^{(p)}(t) = N_0^{(p)} \mathrm{rect}(2\pi f t) \tag{5.8}$$

with

$$\mathrm{rect}(2\pi f t) = \begin{cases} +1, & \text{if } \sin(2\pi f t) \geq 0 \\ -1, & \text{if } \sin(2\pi f t) < 0 \end{cases} .$$

This type of excitation has already been investigated in literature [3]. We want to further examine the dynamics of the plate and the reasoning behind it. We therefore inspect the two simple time series shown in figure 5.19. A sinusoidal excitation and a rectangular one are each shown on the left, and the bifurcation diagram is shown on the right. Both signals have the same amplitude, which is $0.78\,\mathrm{N_{cr}}$. The interesting thing about the applied signal is how it changes the effective stress. The stress in the plate is based on the pre-stress, the parametric stress induced by the excitation, and finally, the stress induced by noise. The blue line in the figures illustrates the stress change based on the applied excitation. The positively displayed pulses make the effective stress higher, thereby getting closer to other modes achieving stable states. The negative pulses, on the other hand, push the effective stress below the critical stress and, therefore, result in no modes having stable states other than zero deflection whatsoever. This can be observed in the graphs as the first mode moves around the stable state. Depending on the momentum with which the deflection of the mode ends up when switching back to the negative wave, the mode gets into a stable state again.

Lastly, we examine a snap-through map of the rectangular excitation (figure 5.20). Compared to the results of the sinusoidal excitation, the snap-throughs appear to occur more quickly. Other than that, the general form of the map with three main tongues and the frequencies are quite similar. Additionally, the influence of noise seems to be the same.

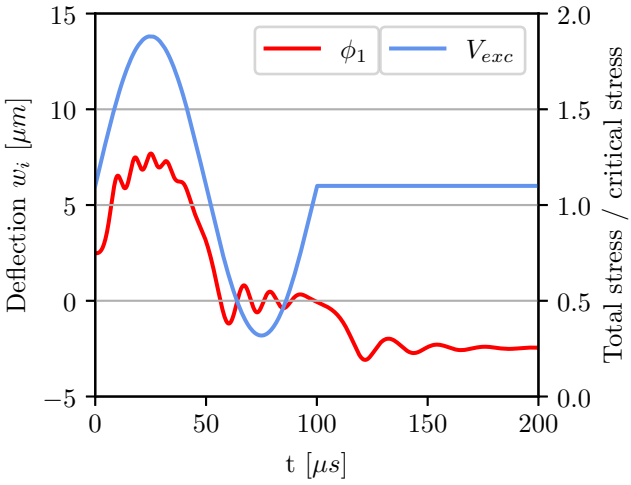

(a) Sinusoidal excitation

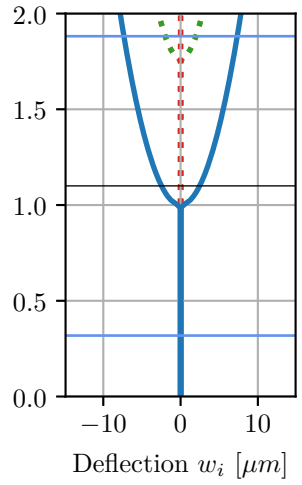

(b) Bifurcation diagram

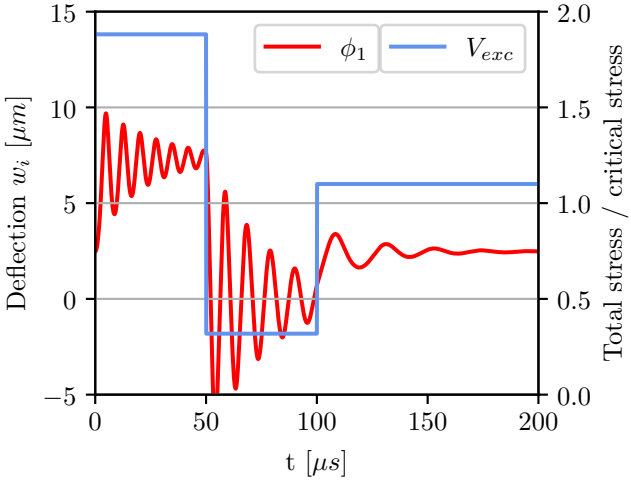

(c) Rectangular excitation.

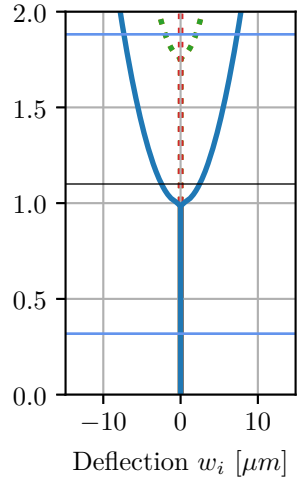

(d) Bifurcation diagram.

Figure 5.19: Time series of rectangular and sinusoidal excitation versus bifurcation diagram. The blue horizontal lines in the bifurcation diagrams indicate the amplitudes of stress reached by the external excitation. The negative pulse leads to a stress of under 0.5, which leads to the first mode having no stable deflection other than zero.

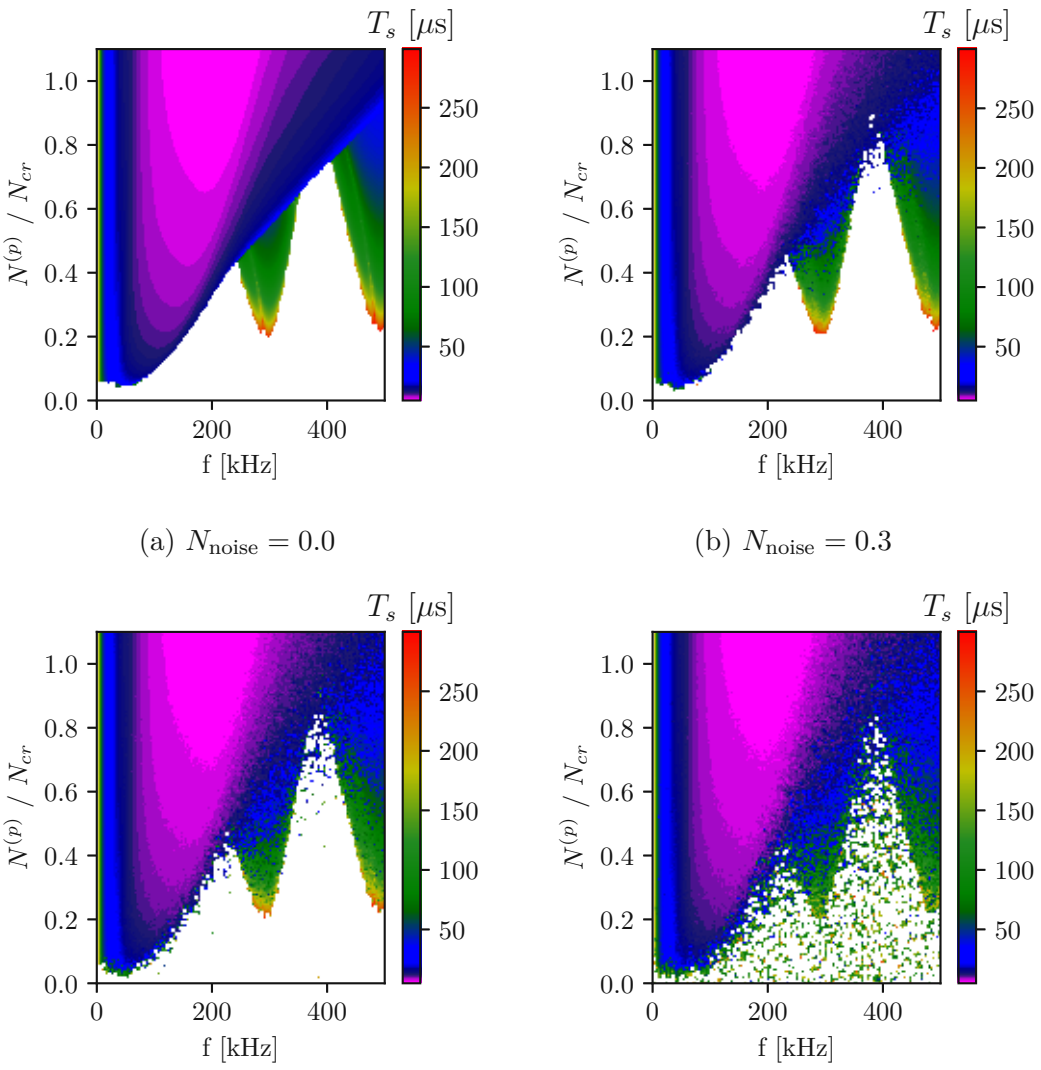

(a) $N_{\text{noise}} = 0.0$

(b) $N_{\text{noise}} = 0.3$

(c) $N_{\text{noise}} = 0.5$

(d) $N_{\text{noise}} = 0.7$

Figure 5.20: Snap-through maps for rectangular excitation and different noise intensities. $N_0 = 1.1\,\mathrm{N_{cr}}$

5.4.3 Comparison With Measurement Results - An Outlook

Moving forward, the next steps will be to further analyse the stochastic behaviour of bistable MEMS plates by making real-life experiments. As shown in literature [2], measurements have already been taken on circular plates. Therefore, adjusting the model's geometry would be needed to try to compare the measured behaviour

with simulation.

Concerning the work done in this thesis, an interesting aspect for future measurements would be analysing the stochastic behaviour of the plates. To achieve this, a specific amount of pulses could be applied, and the final deflection could be measured, similar to the approach taken in [2]. Repeating these measurements multiple times would result in a probability distribution, that highlights the stochastic behaviour of the MEMS plates. Such a result has already been shown in the introduction in figure 1.1.

The following figures illustrate examples from simulations. Figure 5.21 shows the probability of the plate having changed its state after having applied one sine pulse for different noise intensities. This probability is based on ten simulation runs, which only provides us a qualitative understanding. Remembering the influence of the used noise term, as shown in section 3.3, N_{noise} is multiplied with the random variable and therefore changes its variance. To get a feeling of how high the considered noise is, we follow the approach presented in section 3.5. $N_{\text{noise}} = 1 = 1.5 \times 10^{-2}\,\text{N}_{\text{cr}}$ results in a voltage of 0.154 V. Comparing the stress resultants with the ones used in the previous sections, they are about a thousand times smaller.

As expected, there are areas with a 100% probability of either switching or not. There are smaller areas that show the influence of the considered noise. This is particularly visible on the edges, which grow regarding their occupied area for higher noise intensities. This meets expectations, as it is more probable for noise to change the outcome when just slightly altering the excitation amplitude leads to a different result. Noise-robust operation would have to take place in the 100% areas as far away from the edges as possible. Additionally, these noisy areas grow for higher noise intensities, merging not only into the areas no snap happens, but also making these 100% areas smaller.

Furthermore, figure 5.22 shows the same for a different amount of pre-stresses. Although a change in the structure is clearly visible, the impact of noise itself does not seem to play a highly significant role. Based on the results for the snap-through time, we concluded that the influence of noise decreased for higher pre-stress. Comparing figures 5.22a and 5.22d, a difference can be seen at higher frequencies.

Finally, figure 5.23 illustrates the percentage of state switching for a different amount of pulses. The results demonstrate how the complexity of the behaviour increases with a higher number of pulses. With more complex behaviour, the changes induced by the stress also rise accordingly. With the noise impact rising that fast, noise-robust operation is only possible for a very low number of periods.

In conclusion, we investigated the behaviour of noise on the final deflection after a defined amount of excitation pulses. Our results indicate how the influence of

noise is shown on the boarders of a final state change or not. This noise induced areas on the boarders grow for higher noise intensities. However, big changes in the impact of noise can not be seen for different pre-stresses. As the complexity of the resulting map rises for a higher number of pulses, the impact of noise also grows.

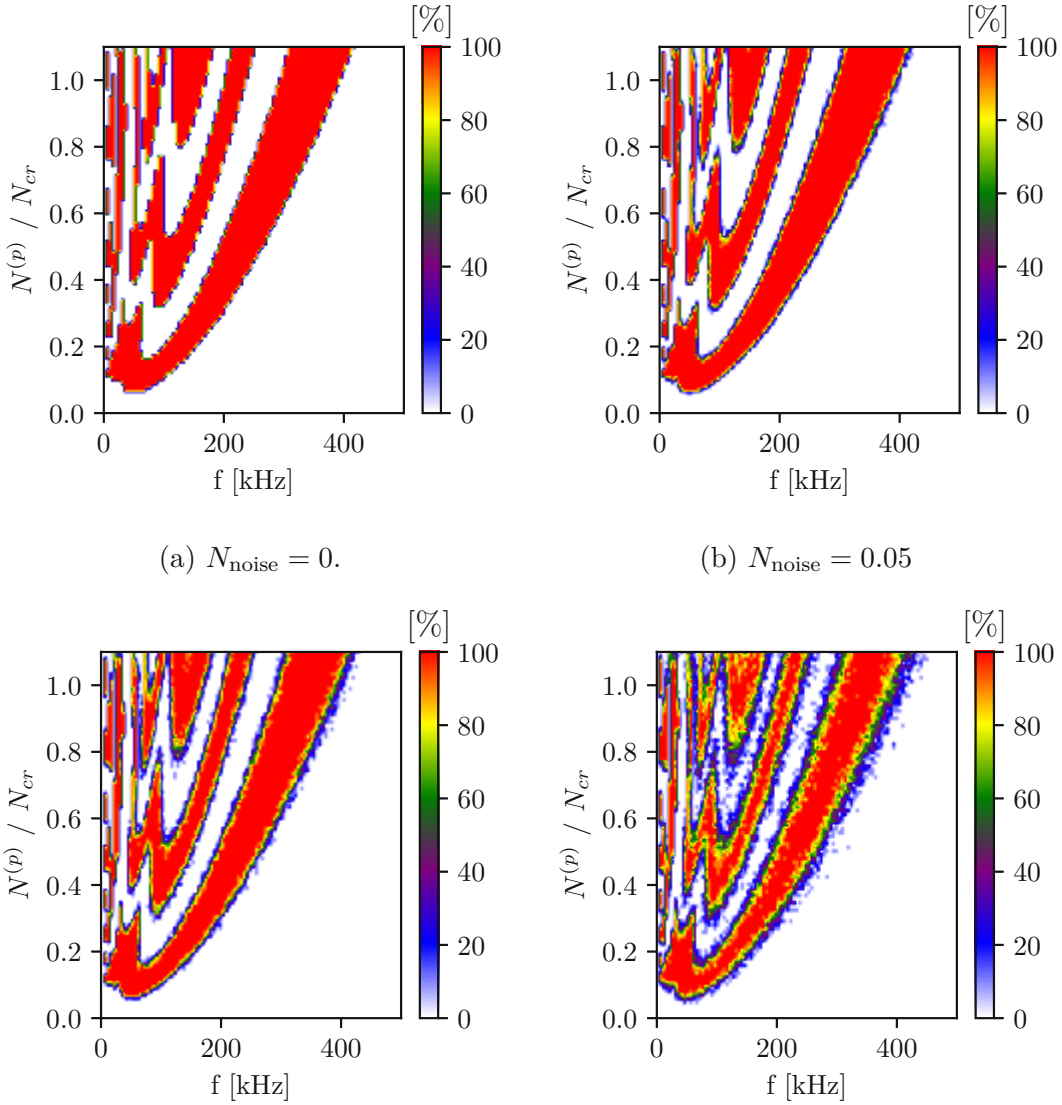

(a) $N_{\text{noise}} = 0.$

(b) $N_{\text{noise}} = 0.05$

(c) $N_{\text{noise}} = 0.1$

(d) $N_{\text{noise}} = 0.2$

Figure 5.21: Maps showing the state change percentage for a different amount of noise with varying frequency and amplitude. $N_0 = 1.1\,\mathrm{N_{cr}}$, 1 pulse.

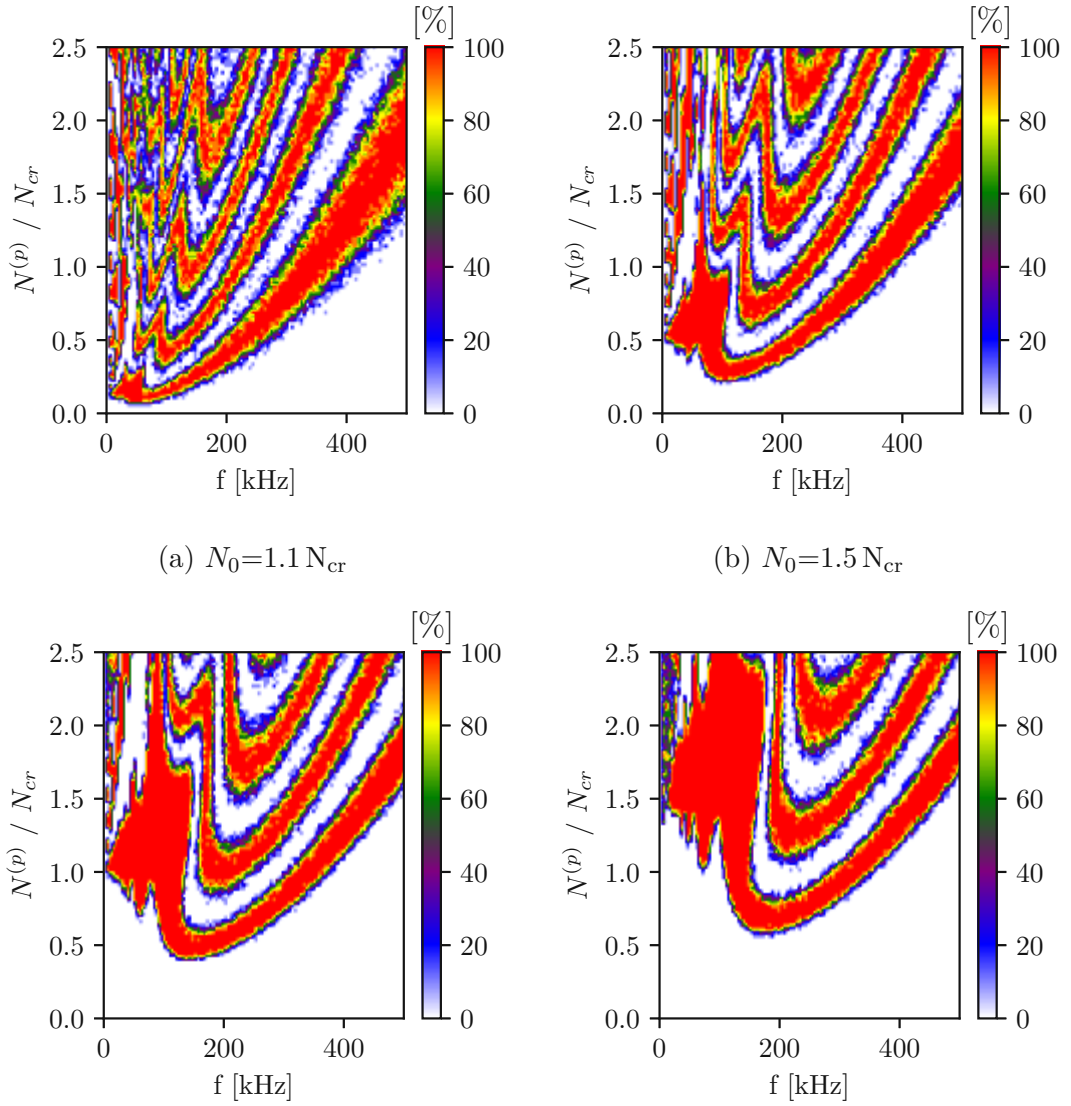

(a) N_0=1.1 N_{cr}

(b) N_0=1.5 N_{cr}

(c) N_0=2.0 N_{cr}

(d) N_0=2.5 N_{cr}

Figure 5.22: Maps showing the state change percentage for a different amount of pre-stress with varying frequency and amplitude. 1 pulse, $N_{noise} = 0.2$.

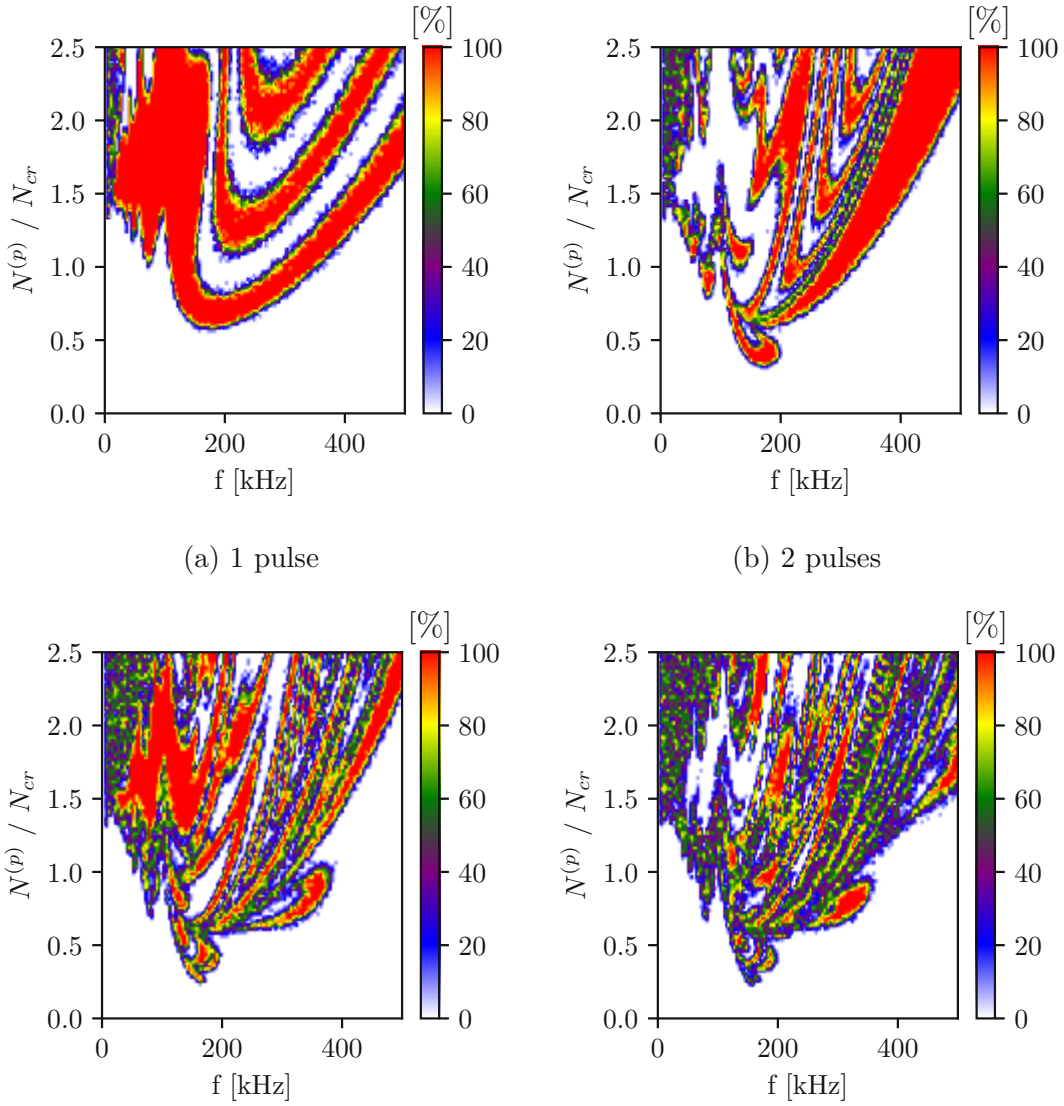

(a) 1 pulse

(b) 2 pulses

(c) 3 pulses

(d) 4 pulses

Figure 5.23: Maps showing the state change percentage for a different amount of pulses with varying frequency and amplitude. $N_0 = 2.5\,\mathrm{N_{cr}}$, $N_{\mathrm{noise}} = 0.2$.

Chapter 6

Conclusion and Outlook

In this study, we examined the influence of noise on the dynamic behaviour of bistable MEMS plates. We extended an existing model by adding noise terms, resulting in a stochastic differential equation. We introduced two noise terms into the model: noise induced by the environment temperature and noise in the piezo layer, which affects the mechanical stress in the plates. We developed a framework using different numerical solvers to obtain results for the snap-through time. We further investigated approximations of the four mode SDE model by comparing single-shot solutions and numerical results of the Fokker-Planck equation with those resulting of the Monte Carlo simulation. The results showed the reduction in needed computations does not outweigh the resulting inaccuracy. We also investigated the stochastic resonance of the plates and determined the mean escape rate. Finally, we explored how noise affects attempts of switching the plate state by using a small amount of excitation pulses.

Our results indicate that environment temperature does not play a significant role in the dynamics of the plates for the considered geometry. The structures would need to be much smaller to be significantly influenced by temperature. Therefore, the stochastic behaviour previously seen in measurements may have other reasons. Our model shows higher robustness against noise for higher pre-stresses when exploring snap-through times for various excitation frequencies and amplitudes. Noise not only alters the resulting snap-through times, but can also lead to snap-throughs in areas that first appear to be relatively clear of them.

We also discussed how to further develop the model for comparison with experimental data, and what measurements would be of interest in relation to this work. This involves repeated measurements to observe the stochastic behaviour of the bistable plates. When investigating whether the state of the plate changed after excitation for varying excitation amplitude and frequency, results show that noise is primarily visible on the border between the areas with and without snap-through.

For higher noise intensities, this border area grows, expanding into both directions. We also demonstrate that the areas which posses high certainty of either switching or not get smaller for an increasing number of pulses, making a wanted noise robust operation much more challenging.

Looking at the future work in a more general view, artificial intelligence (AI) has a significant role in the field of dynamical systems. AI has been used to solve Fokker-Planck equations using Deep Learning [21], up to predicting noise-induced critical transitions and discovering escape probabilities from raw data [10, 19]. Another interesting approach is the use of noise as a diagnostic tool for quality and reliability of MEMS, abandoning the view of noise as a bad side effect [11].

Appendix

SDE Coefficients

Needed coefficients:

$$M_{ij} = \int_\Omega \phi_i \phi_j d\Omega \tag{1}$$

$$K_{ij} = \int_\Omega \phi_i \left(\phi_{j,\bar{x}\bar{x}\bar{x}\bar{x}} + \left(\frac{L_x}{L_y}\right)^4 \phi_{j,\bar{y}\bar{y}\bar{y}\bar{y}} + 2\left(\frac{L_x}{L_y}\right)^2 \phi_{j,\bar{x}\bar{x}\bar{y}\bar{y}} \right) d\Omega \tag{2}$$

$$C_{ij} = -\left(\frac{L_x}{L_y}\right)^2 \int_\Omega \phi_i \left(\phi_{j,\bar{x}\bar{x}} + \phi_{j,\bar{y}\bar{y}}\right) d\Omega \tag{3}$$

$$G_{ijkl} = -\left(\frac{L_x}{L_y}\right)^2 f_{jkm} \int_\Omega \phi_i \left(\phi_{m,\bar{y}\bar{y}}\phi_{l,\bar{x}\bar{x}} + \phi_{m,\bar{x}\bar{x}}\phi_{l,\bar{y}\bar{y}} - 2\phi_{m,\bar{x}\bar{y}}\phi_{l,\bar{x}\bar{y}}\right) d\Omega \tag{4}$$

$$f_{ijk}\left(F^{(1)}_{kk} + \left(\frac{L_x}{L_y}\right)^4 F^{(2)}_{kk} + 2\left(\frac{L_x}{L_y}\right)^2 F^{(3)}_{kk}\right) = 12(1-\mu^2)\left(\frac{L_x}{L_y}\right)^2 \left(F^{(4)}_{ijk} - F^{(5)}_{ijk}\right) \tag{5}$$

$$F^{(1)}_{kl} = \int_\Omega \phi_{k,\bar{x}\bar{x}\bar{x}\bar{x}} \phi_l d\Omega \tag{6}$$

$$F^{(2)}_{kl} = \int_\Omega \phi_{k,\bar{y}\bar{y}\bar{y}\bar{y}} \phi_l d\Omega \tag{7}$$

$$F^{(3)}_{kl} = \int_\Omega \phi_{k,\bar{x}\bar{x}\bar{y}\bar{y}} \phi_l d\Omega \tag{8}$$

$$F^{(4)}_{kl} = \int_\Omega \phi_{i,\bar{x}\bar{y}} \phi_{j,\bar{x}\bar{y}} \phi_l d\Omega \tag{9}$$

$$F^{(4)}_{kl} = \int_\Omega \phi_{i,\bar{x}\bar{x}} \phi_{j,\bar{y}\bar{y}} \phi_l d\Omega \tag{10}$$

List of Figures

List of Tables

Listings

Acronyms

MEMS Micro-Electro-Mechanical Systems

SDE Stochastic Differential Equation

Bibliography

[1] A. Bulsara and L. Gammaitoni. Tuning in to Noise. *Physics Today*, 49(3):39–45, 03 1996.

[2] M. Dorfmeister, B. Kössl, M. Schneider, G. Pfusterschmied, and U. Schmid. Switching performance of bistable membranes activated with integrated piezoelectric thin film transducers. *Journal of Micromechanics and Microengineering*, 29(10):105008, 08 2019.

[3] J. Fabian. *Numerical simulation of parametrically excited bistable MEMS plates*. Vienna, 2022.

[4] O. Foupouapouognigni, C. Nono Dueyou Buckjohn, M. Siewe Siewe, and C. Tchawoua. Hybrid electromagnetic and piezoelectric vibration energy harvester with gaussian white noise excitation. *Physica A: Statistical Mechanics and its Applications*, 509:346–360, 2018.

[5] C. Gardiner. *Stochastic Methods: A Handbook for the Natural and Social Sciences*. Springer Series in Synergetics. Springer Berlin Heidelberg, 2010.

[6] C. Herbert and F. Bouchet. Predictability of escape for a stochastic saddle-node bifurcation: when rare events are typical. *Phys. Rev. E*, 96:030201(R), 2017.

[7] D. Higham. An algorithmic introduction to numerical simulation of stochastic differential equations. *SIAM Review*, 43:525–546, 09 2001.

[8] O. Ibe. *Elements of Random Walk and Diffusion Processes*. John Wiley & Sons, Ltd, 2013.

[9] K. Jacobs. *Stochastic Processes for Physicists: Understanding Noisy Systems*. Cambridge University Press, 2010.

[10] J. Ma, Y. Xu, Y. Li, R. Tian, and J. Kurths. Predicting noise-induced critical transitions in bistable systems. *Chaos: An Interdisciplinary Journal of Nonlinear Science*, 29(8):081102, 08 2019.

[11] F. Mohd-Yasin and D. Nagel. Noise as diagnostic tool for quality and reliability of mems. *Sensors*, 21:1510, 02 2021.

[12] K. D. Murphy, L. N. Virgin, and S. A. Rizzi. The Effect of Thermal Prestress on the Free Vibration Characteristics of Clamped Rectangular Plates: Theory and Experiment. *Journal of Vibration and Acoustics*, 119(2):243–249, 04 1997.

[13] D. Platz, J. Fabian, E. Samm, M. Mortada, M. Schneider, and U. Schmid. Exploiting parametric instability in bistable mems actuators. In *2023 IEEE 36th International Conference on Micro Electro Mechanical Systems (MEMS)*, pages 530–533, 2023.

[14] S. Rajasekar and M. Sanjuán. *Nonlinear Resonances*. Springer Cham, 01 2016.

[15] A. J. Roberts. Modify the improved euler scheme to integrate stochastic differential equations, 2012.

[16] K. Schmitz-Abe and W. Shaw. Measure order of convergence without an exact solution, euler vs milstein scheme. *International Journal of Pure and Applied Mathematics*, 24, 01 2005.

[17] H. Shih-Wei. 2d_fpe_solver. `https://github.com/b03901165Shih/2D_FPE_Solver`, 2019.

[18] A. Tocino and R. Ardanuy. Runge–kutta methods for numerical solution of stochastic differential equations. *Journal of Computational and Applied Mathematics*, 138(2):219–241, 2002.

[19] D. Wu, M. Fu, and J. Duan. Discovering mean residence time and escape probability from data of stochastic dynamical systems. *Chaos: An Interdisciplinary Journal of Nonlinear Science*, 29(9):093122, 09 2019.

[20] T. Yang, L. Jiye, and C. Qingjie. Response analysis of the archetypal smooth and discontinuous oscillator for vibration energy harvesting. *Physica A: Statistical Mechanics and its Applications*, 507:358–373, 2018.

[21] X. Yong, Z. Hao, L. Yongge, Z. Kuang, L. Qi, and K. Jürgen. Solving fokker-planck equation using deep learning. *Chaos: An Interdisciplinary Journal of Nonlinear Science*, 30(1), 01 2020.